


Enhanced Activation of HCN Channels Reduces Excitability and Spike-Timing Regularity in Maturing Vestibular Afferent Neurons

Christopher M. Ventura¹ and  Radha Kalluri^{1,2,3}

¹Neuroscience Graduate Program, ²Department of Otolaryngology-Head and Neck Surgery, Keck School of Medicine, and ³Zilkha Neurogenetic Institute, Keck School of Medicine, University of Southern California, Los Angeles, California, 90057

Vestibular ganglion neurons (VGNs) transmit information along parallel neuronal pathways whose signature distinction is variability in spike-timing; some fire at regular intervals while others fire at irregular intervals. The mechanisms driving timing differences are not fully understood but two opposing (but not mutually exclusive) hypotheses have emerged. In the first, regular-spiking is inversely correlated to the density of low-voltage-gated potassium currents (I_{KL}). In the second, regular spiking is directly correlated to the density of hyperpolarization-activated cyclic nucleotide-sensitive currents (I_H). Supporting the idea that variations in ion channel composition shape spike-timing, VGNs from the first postnatal week respond to synaptic-noise-like current injections with irregular-firing patterns if they have I_{KL} and with more regular firing patterns if they do not. However, *in vitro* firing patterns are not as regular as those *in vivo*. Here we considered whether highly-regular spiking requires I_H currents and whether this dependence emerges later in development after channel expression matures. We recorded from rat VGN somata of either sex aged postnatal day (P)9–P21. Counter to expectation, *in vitro* firing patterns were less diverse, more transient-spiking, and more irregular at older ages than at younger ages. Resting potentials hyperpolarized and resting conductance increased, consistent with developmental upregulation of I_{KL} . Activation of I_H (by increasing intracellular cAMP) increased spike rates but not spike-timing regularity. In a model, we found that activating I_H counter-intuitively suppressed regularity by recruiting I_{KL} . Developmental upregulation in I_{KL} appears to overwhelm I_H . These results counter previous hypotheses about how I_H shapes vestibular afferent responses.

Key words: cAMP; I_H ; I_{KL} ; neuronal excitability; spike-timing regularity; vestibular ganglion

Significance Statement

Vestibular sensory information is conveyed on parallel neuronal pathways with irregularly-firing neurons encoding information using a temporal code and regularly-firing neurons using a rate code. This is a striking example of spike-timing statistics influencing information coding. Previous studies from immature vestibular ganglion neurons (VGNs) identified hyperpolarization-activated mixed cationic currents (I_H) as driving highly-regular spiking and proposed that this influence grows with the current during maturation. We found that I_H becomes less influential, likely because maturing VGNs also acquire low-voltage-gated potassium currents (I_{KL}), whose inhibitory influence opposes I_H . Because efferent activity can partly close I_{KL} , VGN firing patterns may become more receptive to extrinsic control. Spike-timing regularity likely relies on dynamic ion channel properties and complementary specializations in synaptic connectivity.

Introduction

The vestibular system sends information from the sensory periphery to the brainstem along parallel neuronal pathways whose

signature distinction is a striking difference in spike-timing statistics. Spikes occur at regular intervals in one path and at irregular (noisy) intervals in the other (Baird et al., 1988; for review, see Goldberg, 2000). Spike-timing regularity correlates with other important features of the neuronal response, such as gain, phase, and sensitivities to different frequencies of head motion

Received July 13, 2018; revised Jan. 14, 2019; accepted Jan. 19, 2019.

Author contributions: C.M.V. wrote the first draft of the paper; C.M.V. and R.K. edited the paper; C.M.V. and R.K. designed research; C.M.V. performed research; C.M.V. and R.K. analyzed data; C.M.V. and R.K. wrote the paper.

This work was supported by NIH NIDCD Grants R03 DC012652, DC012652S, and R01 DC015512, and the Department of Otolaryngology at the University of Southern California. We thank Maya Monges-Hernandez for technical assistance, and Alexander Markowitz and Ruth Anne Eatock for commenting on previous versions of the paper.

The authors declare no competing financial interests.

Correspondence should be addressed to Radha Kalluri at radha@usc.edu.
<https://doi.org/10.1523/JNEUROSCI.1811-18.2019>

Copyright © 2019 the authors

(for review, see Goldberg, 2000). It also appears to determine whether these neurons use a rate or temporal code to represent sensory information (Sadeghi et al., 2007). Given its central importance to vestibular function, the aim of our study is to understand the biophysical mechanisms that drive spike-timing regularity.

Pioneering studies considered many mechanisms to explain spike-timing regularity. These included the type and numbers of sensory hair cells contacted by individual neurons, differences in synaptic and/or dendritic morphology, and regional variations in ion channel composition (Smith and Goldberg, 1986; Baird et al., 1988; Fernández et al., 1988, 1990). Ultimately, these studies concluded that variations in ion channel composition are critical for driving differences in spike-timing regularity (Highstein and Politoff, 1978; Smith and Goldberg, 1986; Schessel et al., 1991), but the exact ion channel substrate remains under debate.

Electrophysiological and immunohistochemical data in rats and mice have shown expression for many groups of ion channels, both in the terminals and at the somata of vestibular afferents (Desmadryl et al., 1997; Chabbert et al., 2001; Risner and Holt, 2006; Iwasaki et al., 2008; Kalluri et al., 2010; Lysakowski et al., 2011; Almanza et al., 2012; Horwitz et al., 2014; Yoshimoto et al., 2015). For example, potassium channel expression varies by epithelial zone and could drive zonal variations in spike-timing regularity (Songer and Eatock, 2013; Meredith and Rennie, 2015). Indicative of heterogeneity in ion channel composition, vestibular ganglion neuron (VGN) somata respond with diverse firing patterns when injected with step currents. Somata with large low voltage-gated potassium currents (I_{KL}) respond only at the onset of the current step (transient/phasic), whereas those with little I_{KL} respond with sustained spike trains (sustained/tonic; Fig. 1). When driven with currents that mimic the random timing of synaptic input, transient-spiking VGNs respond with irregularly-timed spike trains, whereas sustained-spiking VGNs respond with more regular patterns (Kalluri et al., 2010). Although these results suggest that I_{KL} can control spike-timing regularity, *in vitro* firing patterns do not have the degree of regularity seen *in vivo*.

Recent studies suggest that highly-regular spiking relies on the depolarizing currents provided by the hyperpolarization-activated cyclic nucleotide (HCN)-sensitive currents (i.e., I_H currents conducted by HCN channels; Horwitz et al., 2014; Yoshimoto et al., 2015). This hypothesis is appealing because I_H produces highly regular auto-rhythmic firing in other systems, famously in sinoatrial node myocytes allowing for pacemaking in the heart (Brown et al., 1979; DiFrancesco, 1981, 2010). Because I_H expression in VGNs grows during development (Yoshimoto et al., 2015) and the current is sensitive to cyclic-nucleotide concentrations (for review, see DiFrancesco, 2010; for VGNs, see Almanza et al., 2012), its influence on spiking could be masked by experimental conditions.

To understand the ion channel substrate necessary for driving variations in spike-timing regularity, we performed *in vitro* whole-cell patch-clamp on isolated VGNs at ages when HCN channel expression has matured and in experimental conditions where the activation of the I_H current is enhanced by increasing intracellular concentrations of cAMP. We report that enhancing I_H increased spike rate, but failed to produce highly regular firing. Using a single compartment model of VGNs, we show that opposing interactions between I_H and I_{KL} currents can explain the lack of highly regular firing.

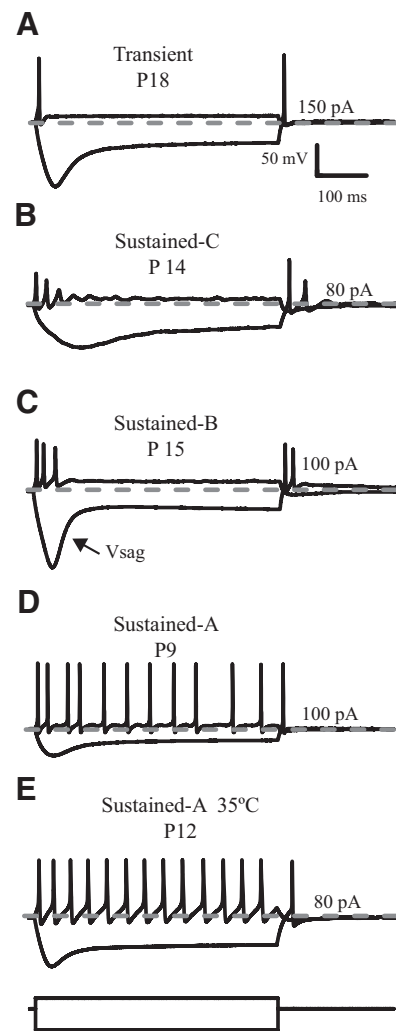


Figure 1. Vestibular ganglion neurons produce different firing patterns in response to depolarizing current steps. **A**, Transient-firing neurons are characterized by a single action potential at the onset of suprathreshold depolarizing steps. **B–D**, Sustained-firing patterns are more variable. **B**, Sustained-C neurons have one or two spikes followed by prominent voltage oscillations. **C**, Sustained-B neurons show adaptation, producing several spikes at current onset and then cease firing (accommodate). **D**, Sustained-A neurons produce long spike trains throughout the current step. **E**, Sustained-A neuron at 35–37°C in 500 μ M db-cAMP, which produces more spikes than in sustained-A neuron shown in **D**. The amplitude of the depolarizing current step that evokes spikes (current threshold) is shown in the label at the right of each trace and the dashed line represents -60 mV. Indicative of the presence of hyperpolarization-activated mixed cationic current (I_H), most VGNs produced a voltage sag (arrow labeled V_{sag}) in response to large hyperpolarizing currents (-200 pA shown). Scale bars (top right trace) apply to all traces. For this figure, recordings were made using whole-cell ruptured-patch with 100 μ M cAMP, except where the recording pipette contained 500 μ M db-cAMP.

Materials and Methods

Preparations

Data were recorded from the superior portion of the vestibular ganglion in Long-Evans rats of either sex aged postnatal day (P)9–21 (P0, birth day). All animals were handled and housed in accordance with National Institutes of Health *Guide for the Care and Use of Laboratory Animals*. All animal procedures were approved by the University of Southern California Institutional Animal Care and Use Committee. Chemicals were obtained from Sigma-Aldrich unless otherwise specified. The temporal bones from the animals were dissected in chilled and oxygenated L-15 supplemented with 10 mM HEPES (Leibowitz medium). The superior part of the vestibular ganglia was detached from the distal and central nerve branches freeing it from the otic capsule. Bone fragments, debris, and any remaining connective tissue were removed from the surface of

the ganglia. Ganglia from 2 to 4 litter-matched animals of either sex were pooled together. Ganglionic tissue was then incubated at 37°C in a solution of L-15 with 0.05% collagenase and 0.25% trypsin for 20–45 min, depending on age of the animal. The ganglia were then washed in fresh L-15 solution, dissociated by triturating through a series of polished Pasteur pipettes and allowed to settle onto poly-D-lysine-coated glass bottom culture dishes (MatTek). Culture dishes contained bicarbonate-buffered culture medium (minimal essential medium, Invitrogen), supplemented with 10 mM HEPES, 5% FBS, and 1% penicillin-streptomycin (Invitrogen). Cells were incubated for 16–24 h in 5% CO₂/95% air at 37°C. Short-term incubation tends to remove supporting and satellite cells, debris from enzyme treatment, and promotes successful recordings as the animals entered the second postnatal week and beyond.

Electrophysiology

Cells were viewed at 400× using an inverted microscope (Zeiss, Axiovert 135 TV) fitted with Nomarski optics. A MultiClamp 700B amplifier, Digidata 1440 board, and pClamp 10.7 software (MDS; RRID: SCR_011323) were used to deliver, record, and amplify all signals. Custom stimuli were generated in MATLAB (MathWorks; RRID: SCR_001622) and delivered via the pClamp software. Recording pipettes were fabricated using filamented borosilicate glass. Pipettes were fire polished to yield an access resistance between 4 and 8 MΩ. Recording pipettes were coated with a silicone elastomer (Sylgard 184; Dow Corning) to reduce pipette capacitance.

The properties of ion channels were studied using whole-cell ruptured-patch or perforated-patch methods. The contents of the standard internal solution contained the following (in mM): 135 KCl, 3.5 MgCl₂, 3 Na₂ATP, 5 HEPES, 5 EGTA, 0.1 CaCl₂, 0.1 Li-GTP, and titrated with 1 M KOH to a pH of 7.35 and an osmolarity of ~300 mmol/kg. Both cAMP and dibutyryl (db)-cAMP were aliquoted and stored as a 10 mM stock at –20°C. Working concentrations were achieved by dilution into the intracellular solution on day of recording. Endogenous conditions were studied using the perforated patch-clamp method where the intracellular milieu is relatively unchanged. The contents of the perforated-patch internal solution contained the following (in mM): 75 K₂SO₄, 25 KCl, 5 MgCl₂, 5 HEPES, 5 EGTA, 0.1 CaCl₂, and titrated with 1 M KOH to a pH of 7.4. Amphotericin B (240/ml; Sigma-Aldrich) was dissolved in DMSO and added to the perforated-patch solution on day of recording. This allowed passage of small monovalent ions while preventing larger molecules from dialyzing.

The series resistance ranged between 8 and 35 MΩ (higher values for perforated patch) and was compensated by 70 and 50%, respectively, giving final resistances between 2.5 and 17 MΩ. Uncompensated resistance was corrected off-line. Recordings were made at room temperature (25–27°C), unless otherwise stated, and in an external bath continuously perfused with fresh oxygenated L-15 media. Standard internal solution and perforated patch internal solution had junction potentials of +4.3 and +5.0 mV, respectively. In some experiments the bath was heated to between 35°C and 37°C with a heated platform and temperature controller (TC-344B; Warner Instruments). To maintain bath temperature with stability, room humidity was maintained using a bench-top humidifier. Junction potentials were computed with JPCalc (Barry, 1994) as implemented in pClamp 10.7 and not corrected for. Only recordings in which the cell had formed a gigaohm seal and maintained stable membrane potential were used. The stability of neurons was monitored by measuring resting potential, input resistance, firing patterns, and in some neurons the activation properties of I_H, at regular intervals throughout the recording period.

Pharmacology

I_H antagonists. A stock solution of ZD7288 was stored at –20°C in 10 mM aliquots. An 80 μM working concentration was achieved by dilution in either L-15 for extracellular administration or in standard internal solution for intracellular administration. A 2 mM stock solution of CsCl in L-15 was prepared fresh on the day of recording for extracellular administration. Drugs were applied via a pressurized super-perfusion system (Warner Instruments). Measurements of I_H were made at least 2–5 min after exposure to the drug.

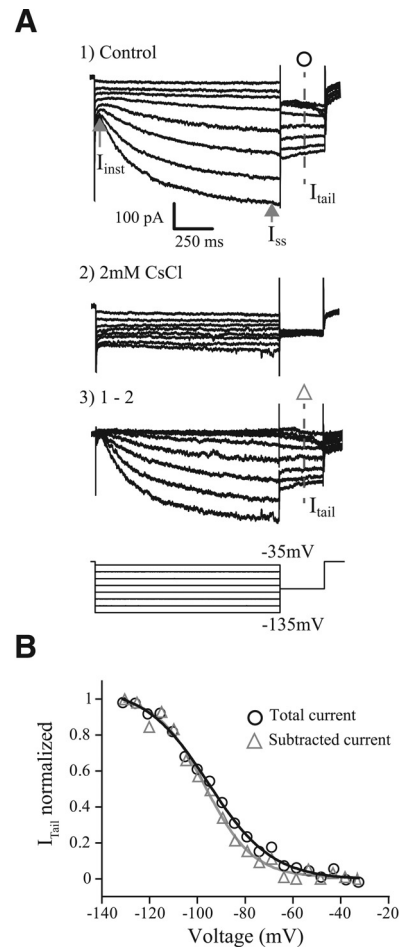


Figure 2. An electrophysiological and pharmacological method for characterizing the activation properties of I_H. Current excited by a family of long duration (1.7 s) conditioning voltage steps ranging from –135 to –35 mV in 5 mV increments followed by a 300 ms tail step to –100 mV. For clarity, not every voltage-step response is shown. Current under control conditions (**A1**) and with CsCl (**A2**) and the Cs⁺-sensitive current obtained by subtraction 1–2 (**A3**). Gray arrows, The amplitude of the I_H current was determined by taking the difference between the I_{inst} and the I_{ss}. **B**, The voltage-dependent activation of I_H is determined by plotting the magnitude of the tail current (I_{tail}) as a function of the conditioning voltage. Curves were fit by a Boltzmann function and normalized by the maximum current. The fits generated from the tail of the control condition (○) and from the current isolated from the Cs⁺-induced block (△) are similar. All voltage-dependent characterization of I_H in subsequent figures is derived from the control condition.

Analysis

General. All data were analyzed with pClamp 10 software (Clampfit; MDS Analytical Technologies). Input resistance (R_{in}) was calculated from voltage changes in response to a hyperpolarizing 10 or 20 pA step of current. The membrane time constant (τ_m) was acquired by fitting the resulting voltage response with a single exponential. Membrane capacitance (C_m) was computed as the ratio of membrane time constant and input resistance (τ_m/R_{in}).

Statistical analysis was done with Origin Pro (OriginLab; RRID: SCR_014212) and/or JMP Pro 13 (SAS Institute; RRID: SCR_014242). Statistical significance was estimated with Student's *t* test when variances were equal or with Welch's *t* test when variances were not equal. We used an α level of 0.05 for all statistical tests. One-way and two-way ANOVAs were applied followed by a *post hoc* Tukey's HSD analysis, as required, to examine the influence of cAMP concentration/condition on I_H half activation, firing rate and coefficient of variation (CV). Statistics are reported as means ± SEM.

I_H activation parameters. We studied the voltage-dependent activation of I_H using a voltage-clamp tail-current protocol (Fig. 2). The HCN

channel that carries I_H opens very slowly and the voltage-dependent activation of I_H is sensitive to the length of hyperpolarization. We designed a protocol that allowed ample time for the channel to activate and provided an accurate measurement of the voltage-dependent activation. The challenge is that neurons can die when held at hyperpolarized voltages for extended periods of time. The protocol begins with a preconditioning voltage step, then a -100 mV “tail-step” for 300 ms and finally returns to -60 mV for 100 ms. The precondition voltage step is incremented by 5 mV to range between -135 and -40 mV. A 15 s delay was implemented between each step to allow enough time for HCN channels to close completely before starting the next voltage step. Several preconditioning lengths were tested (1.25, 1.7, and 2.5 s). Although the 2.5 s protocol provided the most depolarized measures of voltage-dependent activation and had the most complete I_H activation, we found that 1.7 s provided comparable results without killing the neuron. The voltage-dependent activation of I_H is characterized by plotting the currents flowing during the tail step (I_{tail}) against the precondition voltage (V_{pre}). These data were well fit with a Boltzmann function (Eq. 1):

$$I_{tail} = \frac{I_{max}}{1 + \exp\left(\frac{V_{1/2} - V_{pre}}{k}\right)} + C, \quad (1)$$

where I_{max} is the maximum current measured during the tail, V_{pre} is the preconditioning/test voltage, $V_{1/2}$ is the half-activation potential, k is the slope factor, and C is a constant. Measurements of I_{tail} were taken 100 ms into the tail step to avoid contamination from other low-voltage-gated currents, particularly during the most positive voltage steps (-60 to -40 mV) and when I_H was activated with cAMP/db-cAMP.

The voltage-dependent time course for I_H was estimated by fitting the current evoked at the -135 mV preconditioning step with a single exponential. All fits were obtained after a 60 ms delay from the start of the voltage step. Only fits with a correlation coefficient ≥ 0.985 were retained. Mean τ values from the single exponential fit at -135 mV were $\sim 327.9 \pm 30.7$ ms ($n = 20$), which are consistent with those reported by Almanza et al. (2012) in VGNs. We also tried fitting with the sum of two exponentials, which improved fits for nearly 80% of cells at -135 mV (Almanza et al., 2012; Liu et al., 2014), but this type of fit failed more often at depolarized potentials. To yield consistent fits as a function of voltage, we relied on the single exponential fits, which were uniformly good for all cells and voltages.

Pseudo-synaptic stimuli

To mimic natural synaptic input, we generated trains of simulated EPSCs (pseudo-EPSCs) with pseudorandom timing, as previously described by Kalluri et al. (2010). A stimulus set of 20 pseudo-EPSC sweeps was created and delivered to each VGN in current-clamp mode to drive spiking. Spikes were detected with the built-in spike thresholding algorithms of Clampfit 10.7.

For each neuron the CV gives a measure of the spike-timing regularity. CV is computed as the SD of the interspike interval (ISI) divided by the mean ISI. Only CV values for neurons in which the SEM spike rate was $< 10\%$ of the mean ISI were included. CV is inherently related to spike rate (Goldberg et al., 1990a). The normalized statistic CV^* is often used to account for this relationship (Goldberg et al., 1990a). CV^* is the CV at a standard spike rate and allows for a measure of regularity independent of spike rate. We did not use CV^* , choosing instead to only compare CVs of neurons that were driven at the same mean spike rate.

Variations in spike rate were achieved by increasing or decreasing the mean amplitude of the pseudo-EPSCs. Although effective in changing spike rate, this is not a completely natural method of stimulation. A more natural stimulus would modulate both EPSC amplitude and EPSC rate. This stimulation method was chosen to maintain timing patterns (by maintaining a standard EPSC rate) to isolate the influence of ion channels from synaptic input.

Vestibular model

A single compartment conductance-based model was used to test the influence of I_H and I_{KL} on firing patterns. The model was implemented in

Table 1. Model Parameters for r_∞ and τ , selected from our experimental data

	Min activation, 100 μ M cAMP	Max activation, 500 μ M dB-cAMP	Heated max- activation, 500 μ M dB-cAMP + 35°C
$V_{1/2}$, mV	94.11	84.37	85.38
k , slope	8.1	8.6	8.8
a , mV	86.862	80.646	70.911
b , mV	5.768	6.916	12.071
c	3393.342	2551.988	1569.342
d , mV	6.674	14.881	3.769
e	295.958	209.479	149.331

Table 2. Model parameters

	g_{max} , mS/cm ²	$V_{1/2}$, mV	Slope
g_{KH}	2.8	-15	5
g_{leak}	0.03		8
g_{KL}	0–1.1	-44.5	8.8
g_{Na} activation	13 and 20	-38	7
g_{Na} inactivation	3393	-65	6
g_H	0.91	-84 to -96	8.1–8.6

Table 3. Additional model parameters

E_K	-81 mV
E_{Na}	82 mV
E_{leak}	-65 mV
E_H	-46 mV
C_m	0.9 pF/cm ²

MATLAB as a differential equation in which the net current across the neuronal membrane was taken as the sum of currents flowing through individual circuit elements connected in parallel (see Eq. 8).

$$I_{inj} = C_m S \frac{dV}{dt} + I_{KL} + I_{KH} + I_{Na} + I_H + I_{leak}. \quad (2)$$

The currents were driven by the following five ionic conductances: sodium (g_{Na}), low-voltage-gated potassium (g_{KL}), high-voltage-gated potassium (g_{KH}), hyperpolarization-activated mixed cationic (g_H), and leak (g_{leak}). This model is an extension of the single-compartment VGN model previously described by Hight and Kalluri (2016). Here we varied the conductance density, voltage-activation range, and kinetics of the I_H current to mimic the influence of cAMP, as described by the *in vitro* characterizations in this study. In addition, we expanded on the previous description of g_{KL} to include both a Kv1-like and Kv7-like components.

Hyperpolarization-activated cyclic nucleotide-gated mixed-cationic current. Equations 3 through 5 governed the voltage-dependent kinetics of I_H :

$$I_H = \bar{g}_h r^3 S (V - E_h), \quad (3)$$

$$r_\infty = \left[1 + \exp\left(\frac{V + V_{1/2}}{k}\right) \right]^{-1} \quad (4)$$

$$\tau_r = \frac{\{(\exp[-(V + a)/b])^{-1} + \exp[V + a)/d]\}}{c} + e. \quad (5)$$

Cell surface area (S) was fixed to yield a net capacitance of 10 pF. Conductance density (\bar{g}_h), reversal potential (E_h), half-activation voltage $V_{1/2}$, slope factor k , and voltage-dependent activation kinetics (τ_r) were based on experimentally derived values from this study. Half-activation voltage and activation kinetics were defined for two conditions; 100 μ M cAMP and 500 μ M dB-cAMP, which respectively represent minimum and maximum activation conditions. The parameter values for $V_{1/2}$, k , a and e are summarized in Table 1. Conductance densities and other model parameters are summarized in Tables 2 and 3.

Low-voltage-gated K^+ currents. Equations 6 through 8 governed the voltage-dependent activation kinetics of I_{KL} :

$$I_{KL} = (\gamma_{kv1}\bar{g}_{KL}w_{kv1}^4Z_{kv1} + \gamma_{kv7}\bar{g}_{KL}w_{kv7}^4Z_{kv7})S(V - E_K). \quad (6)$$

I_{KL} was driven in part by Kv1-like and Kv7-like conductances and γ_{kv1} and γ_{kv7} defined the fraction of total conductance contributed by each of the two components. The variables w and z represent activation and inactivation kinetics. The inactivation kinetics were adjusted to reflect the inactivation present in Kv1 channels and the lack thereof in Kv7 channels. The Kv1 component was modeled to activate nearly 10 times faster than the Kv7 component (compare Eqs. 7, 8):

$$\tau_{w_{kv1}} = 100\{6 \exp[(V + 60)/6] + 16 \exp[-(V + 60)/45]\}^{-1} + 1.5, \quad (7)$$

$$\tau_{w_{kv7}} = 1000\{6 \exp[(V + 60)/6] + 16 \exp[-(V + 60)/45]\}^{-1} + 1. \quad (8)$$

Model implementation. The model was implemented in MATLAB 2016b running on a Windows 10 operating system. The differential equation (Eq. 2) for the membrane voltage, $V(t)$, was numerically solved using a backward difference method. The associated code is accessible via the ModelDB repository at <http://senselab.med.yale.edu/ModelDB/showModel.cshtml?model=244202>.

Results

Whole-cell patch-clamp recordings were made by either ruptured-patch or perforated-patch methods in isolated vestibular ganglion neurons (VGN) from rats ranging in age between postnatal day (P)9 through P21 ($n = 146$). First, we describe the basic firing patterns of VGNs during the second and third postnatal weeks. Second, we define the sensitivity of the I_H current in VGNs to modulation by cyclic adenosine monophosphate (cAMP), a well known modulator of HCN channels. Third, we describe the influence of I_H on VGN firing patterns and spike-timing regularity. Finally, we explore the interaction between I_H and I_{KL} using a single compartment conductance-based model for VGN.

Step-evoked firing patterns

We classified neurons into two broad groups based on the firing patterns evoked by depolarizing current injections: *transient-firing* (83 of 146 neurons; Fig. 1A) and *sustained-firing* (63 of 146 neurons; Fig. 1B–D). These classifications are similar to those used by Kalluri et al. (2010) and Iwasaki et al. (2008). Transient-firing neurons displayed strong spike-train accommodation, firing a single spike at the onset of the current step. Beyond spike threshold, the firing pattern of most transient-spiking neurons was invariant to intensity. In a few rare cases, transient-firing neurons fired a second spike when injected with high amplitude currents (4/83 neurons; data not shown). Sustained-firing neurons displayed varying degrees of accommodation, ranging from cells that fired long trains of spikes (sustained-A firing patterns had spikes throughout the depolarizing step; Fig. 1D) to cells with intermediate degrees of accommodation (sustained-B/sustained-C firing patterns had shorter trains of spikes followed by voltage oscillations; Fig. 1C, B, respectively). Consistent with Kalluri et al. (2010), the degree of accommodation depended on intensity for the sustained-firing patterns. Figure 1E shows a sustained-firing pattern at a recording temperature between 35°C and 37°C.

When injected with hyperpolarizing currents, most neurons (140/146) responded with a deep voltage hyperpolarization followed by a slow depolarization that eventually reached steady state (Fig. 1A–D). Such hyperpolarization-induced voltage “sags” indicate the presence of the HCN channel-mediated current, I_H (Fig. 1C; Rennie and Streeter, 2006; Angelo and Margrie, 2011; Almanza et al., 2012). On average, voltage sags increased in amplitude with larger hyperpolarizing current injections and were first visible when the membrane potential fell below -80 mV.

Our goal was to understand how I_H current influences spike-timing regularity. One way to do this is to compare responses before and after selectively blocking the current with channel-specific antagonists such as ZD7288 and CsCl. This approach was not successful here because both antagonists may affect more than just HCN channels. For example, CsCl is known to block other kinds of potassium channels including inward rectifying potassium channels (Bond et al., 1994; Takumi et al., 1995). Previous studies have also shown that ZD7288 can partially block sodium, T-type calcium, and/or potassium channels (Felix et al., 2003; Sánchez-Alonso et al., 2008; Wu et al., 2012). We suspected similar nonspecific effects in VGNs because action potential amplitudes decreased, and net conductance increased when either ZD7288 or CsCl blocked I_H (5 of 8 cells; data not shown). This is a counter-intuitive result since blocking the channel should have decreased net conductance. Although not discussed, a similar effect in VGNs is evident in the recordings presented by Yoshimoto et al., 2015. We concluded that we could not rely on these channel antagonists to isolate the role of I_H on firing patterns. As shown next, we chose to amplify I_H by controlling the intracellular concentration of cAMP, which shifts the current’s voltage activation range (Almanza et al., 2012).

Enhancing the activation of I_H by controlling cAMP concentration

In voltage-clamp, hyperpolarization produced inward currents with a near instantaneous component (I_{ins}) and a slowly activating component that eventually reached steady state (I_{ss} ; Fig. 2A). Known I_H antagonists, CsCl (Fig. 2A2) and ZD7288 (data not shown), blocked the slow current, suggesting that it was HCN mediated. The current’s reversal potential (-32.7 ± 2.8 mV, $n = 8$) and voltage activation range and kinetics (discussed further below; Figs. 2, 3) are consistent with reported values for I_H (Biel et al., 2009; Almanza et al., 2012; Yoshimoto et al., 2015). We measured the activation range of I_H under several experimental conditions. First, we varied the concentration of simple cAMP in the intracellular pipette solution (at 10, 100, 200, and 500 μ M). Second, we used perforated-patch methods (where the intracellular milieu is left intact) to estimate the endogenous concentration of cAMP. Third, we used 100 and 500 μ M db-cAMP, a non-hydrolysable version of cAMP that resists degradation by phosphodiesterases. Fourth, we tested if the activation of I_H is further enhanced by increasing recording temperature, as previously reported in the substantia nigra (Gambardella et al., 2012).

Estimating the voltage-dependent activation of I_H

To estimate the voltage-dependent activation properties of I_H , we used a voltage-clamp tail protocol, which consists of 1.7-s-long preconditioning steps from -135 to -35 mV in 5 mV increments followed by a tail step to -100 mV (Fig. 2A, bottom). The long preconditioning step allowed I_H to approach steady-state activation but was not so long as to kill cells because of prolonged hyperpolarization (see Materials and Methods). The tail step to -100 mV was within the typical activation range for HCN channels but hyperpolarized away from the activation range of most other channels known to be expressed in VGNs (e.g., low-voltage-gated potassium channels). The currents measured during the tail step reflect the channels activated during the preconditioning steps but with a fixed driving force. The maximum current density ($I_{max}/capacitance$) was larger for sustained-firing neurons than for transient-firing neurons (11.8 ± 1.2 pA/pF vs 6.9 ± 0.6

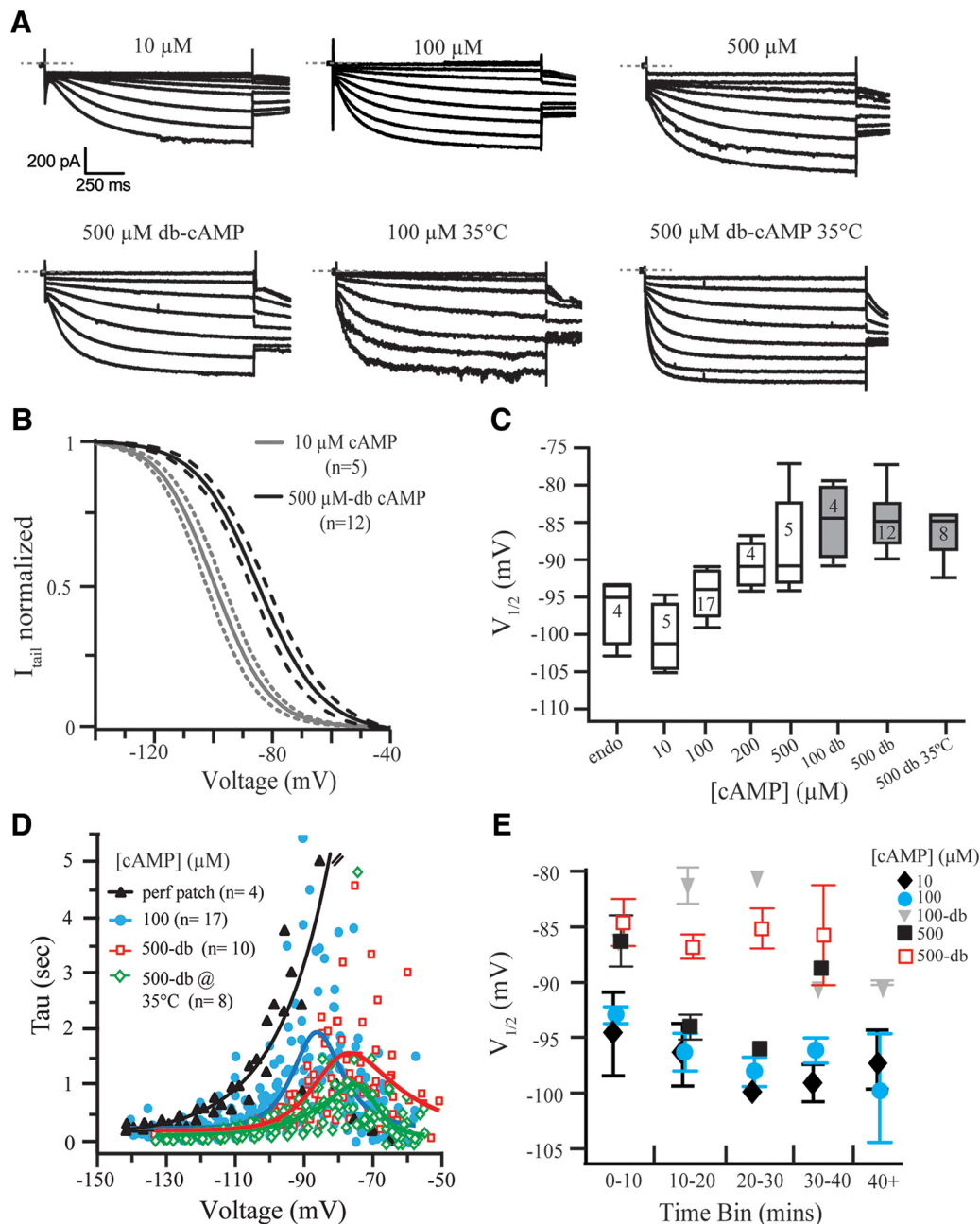


Figure 3. Effects of cAMP concentration and temperature on the activation of I_H currents. **A**, I_H currents activated by a family of voltage steps from -135 to -35 mV under several cAMP concentrations and temperature combinations. As in Figure 2, tail currents were used to construct current–voltage relationships. **B**, Normalized current–voltage relationships (means \pm 95% confidence intervals) for I_H are compared for the $10 \mu\text{M}$ cAMP and $500 \mu\text{M}$ db-cAMP conditions. The difference between the two conditions illustrates the potential range of I_H activation. **C**, Box plots for each cAMP condition. $V_{1/2}$ depolarizes dependent on cAMP concentration, db-cAMP conditions produce the most depolarized $V_{1/2}$ values (shaded box plots). Increasing the concentration of db-cAMP from 100 to $500 \mu\text{M}$ did not further depolarize $V_{1/2}$ and neither did increasing the recording temperature to 35°C . The endogenous concentration was obtained in perforated patch configuration. Mean slope value (k) for all the conditions was $8.3 \pm 0.2 \text{ mV}$ and not affected by cAMP concentration. **D**, A single exponential was used to fit the currents produced by voltage steps from -135 to -65 mV. The time constant of the fits, τ_{single} , is plotted as function of voltage for $100 \mu\text{M}$ cAMP (blue; $n=17$), $500 \mu\text{M}$ db-cAMP (red; $n=10$), perforated patch (black; $n=4$), and $500 \mu\text{M}$ db-cAMP at 35°C (green; $n=8$). Solid lines show fits were produced using Equation 5 to show the relationship of τ_{single} values and voltage. Parameters for the fits at $100 \mu\text{M}$ cAMP, $500 \mu\text{M}$ cAMP, and $500 \mu\text{M}$ db-cAMP at 35°C are summarized in Table 1. **E**, For all conditions except those with db-cAMP, mean $V_{1/2}$ hyperpolarized as a function of time. $V_{1/2} \pm \text{SEM}$ is plotted as a function of recording time for $10 \mu\text{M}$ cAMP (diamonds), $100 \mu\text{M}$ cAMP (cyan circles), $100 \mu\text{M}$ db-cAMP (gray downward triangle), $500 \mu\text{M}$ cAMP (squares), and $500 \mu\text{M}$ db-cAMP (red open squares).

pA/pF; $t_{(25,8)} = -3.6$, $p = 0.0013$, Welch’s unpaired t test), consistent with results reported by Yoshimoto et al. (2015). The normalized tail current ($I_{\text{tail}}/I_{\text{tail}}^{\text{max}}$) is plotted as a function of the preconditioning step to show the voltage-dependent activation of I_H (Fig. 2B). The normalized activation curves generated from these whole-cell currents were similar to those extracted by pharmacologically isolating I_H (Fig. 2B). These results led us to conclude that the tail current measurements were adequate for

characterizing I_H . All subsequent I_H activation parameters are derived from the unblocked whole-cell currents.

Modulating the voltage-dependent activation range of I_H

Examples of whole-cell currents recorded in response to the tail protocol from six cells, each at different intracellular cAMP concentrations and two obtained in 35°C are shown in Figure 3A. The activation curves shifted to more positive potentials as cAMP

concentration increased; nearly 15 mV when two extreme concentrations were compared (10 and 500 μM db-cAMP; Fig. 3B). A similar shift has been reported for auditory afferents in response to cAMP analogues (Yi et al., 2010). We found a significant dependence of $V_{1/2}$ on cAMP condition ($F_{(6,44)} = 11.67$, $p = 0.0001$ based on one-way ANOVA; Fig. 3C). Based on similarity in $V_{1/2}$, we estimate that the endogenous concentration of cAMP (the perforated-patch condition) is between 10 and 100 μM . This estimate is consistent with reports by Almanza et al. (2012). At 100 μM cAMP, the mean $V_{1/2}$ and slope factor (k) are -94.32 ± 3.06 mV and 7.97 ± 1.31 mV ($n = 14$), respectively. This is also consistent with reported values for I_H at 100 μM cAMP (-93 ± 2 and 9 ± 0.9 mV; Almanza et al., 2012). Interestingly, mean $V_{1/2}$ values were not significantly different between the 100 and 500 μM db-cAMP conditions, suggesting that enzymatic degradation of cAMP is a critical parameter affecting cAMP concentration and I_H activation.

Temperature did not further depolarize the activation range of I_H . In the substantia nigra increasing recording temperature depolarizes the activation range of I_H by as much as 15–20 mV (Gambardella et al., 2012). Here we found that recording in 500 μM db-cAMP with an elevated temperature (35°C) did not further depolarize the activation range of I_H (Fig. 3C, compare gray box plots). These results suggest that the db-cAMP is at least as effective at shifting the activation range of I_H as temperature. We did not test the influence of temperature alone on the activation range of I_H , although such a temperature-dependent shift would offer a physiologically plausible mechanism for enhancing I_H .

Modulating the activation time course

Next, we show that the time course of I_H activation speeds up with increased concentrations of cAMP. We applied single exponential fits to the currents evoked by the family of voltage steps from -135 to -55 mV. A single exponential reliably fit our data between -135 and -55 mV. Double exponentials better fit the I_H current at -135 mV (Almanza et al., 2012; Liu et al., 2014) but failed for the smaller hyperpolarizations as the size of I_H current diminished. We relied on single exponential fits because they were robust in all cells and for wide range of voltage steps. In Figure 3D, the exponent τ is plotted as a function of voltage steps for recordings made under the four cAMP conditions (perforated-patch, black triangle; 100 μM cAMP, blue circle; 500 μM -dB cAMP, red square; 500 μM -dB cAMP @ 35°C, green triangles). The voltage-dependent trends for τ activation were fit with Equation 5 (see Materials and Methods) for each cAMP condition (Fig. 3D, solid lines). These same fits were used in the model described later. In each condition, the current activates fastest at extreme hyperpolarizations and slows as the voltage step approaches $V_{1/2}$. As the voltage steps become more positive the activation kinetics speed up. Like the cAMP-dependent shift in voltage activation, the activation kinetics shift such that at any particular voltage (e.g., -90 mV) the 500 μM db-cAMP was the fastest. Similar cAMP driven acceleration in activation kinetics have been reported in various types of neurons including in chick nucleus laminaris, substantia nigra pars compacta and spiral ganglion (Yamada et al., 2005; Yi et al., 2010; Gambardella et al., 2012). Although increasing temperature did not further depolarize half activation voltage beyond that produced by 500 μM db-cAMP (Fig. 3C), it did speed up activation kinetics (Fig. 3D, green symbols).

Time-dependent stability of I_H modulation by cAMP

Although we found that the activation range of I_H could be shifted by increasing cAMP concentration, the shifts were most robust and prolonged in the db-cAMP conditions. Since we were characterizing the activation properties of I_H and firing patterns in the same groups of cells, it was important for us to maintain stability for ~ 30 – 40 min. To determine the time-stability of cAMP driven shift, we measured I_H activation curves at regular time intervals throughout the recording session. Figure 3E shows mean $V_{1/2}$ as a function of recording time and by cAMP condition. For all but the 500 μM db-cAMP condition, the mean $V_{1/2}$ was most depolarized during early recordings (0–10 min) and became progressively more hyperpolarized as neurons were held for longer periods (30–40 min). In Figure 3C, activation parameters of I_H were taken from the earliest recording time possible. In db-cAMP, $V_{1/2}$ values remained time stable, showing no significant difference between early (0–10 min) and late recordings (30–40 min; $t_{(3,3)} = -0.13$, $p = 0.907$, paired t test). This is presumably because db-cAMP is a non-hydrolysable version of cAMP that can maintain elevated intracellular cAMP levels for hours (Campos-Toimil et al., 2008). We did not determine whether db-cAMP remains stable beyond 40 min. The ability to stably shift the activation range of I_H was ultimately important for characterizing the influence of I_H on firing patterns (presented in the next section). Most of our quantitative comparisons are between the 100 μM cAMP condition (which we estimate to be most like the endogenous condition) and the 500 μM db-cAMP condition (where we are confident that I_H activation was the most robust and stable).

Effects of cAMP on firing patterns

Step-evoked firing patterns with increased cAMP

To understand how cAMP driven enhancement of I_H influenced firing patterns, we compared spikes evoked by ~ 100 – 120 pA step currents in 100 μM cAMP ($n = 12$) and 500 μM db-cAMP ($n = 10$). We also recorded at 35°C with 500 μM cAMP ($n = 8$) to test whether increasing temperature together with elevated cAMP concentrations had an additional influence on spike timing. Figure 4, A1 and A2, shows spike traces from example sustained-spiking neurons in the three recording conditions. For each neuron, we quantified the first spike latency (t_p) and the slope of the afterhyperpolarization trajectory (AHP slope; Fig. 4B1,B2, filled symbols are for the examples in A). We applied two-way ANOVAs to test the influence of the three cAMP conditions and firing-pattern category on each of the two spike features. Both, first spike latency and AHP slope were significantly dependent on cAMP condition ($F_{(2,29)} = 4.47$, $p = 0.02$; $F_{(2,30)} = 5.10$, $p = 0.01$, respectively) and AHP slope also depended on firing-pattern ($F_{(1,30)} = 7.58$, $p = 0.01$). *Post hoc* analysis by Tukey HSD indicated that first spike latency tended to be shorter and AHP slopes were steeper in the two 500 μM db-cAMP conditions than in the 100 μM cAMP condition ($p = 0.030$ and $p = 0.086$, respectively, for first spike latency; $p = 0.026$ and $p = 0.031$, respectively, for AHP slope). Neither feature was significantly different between the 500 μM db-cAMP and 500 μM db-cAMP at 35°C conditions ($p = 0.96$ for first spike latency; $p = 0.99$ for AHP slope). These results suggest that more I_H current was available in elevated cAMP to speed up afterhyperpolarization trajectories and spike timing, but that raising temperature had no additional influence on these two spike features (Fig. 4B,D).

Noise (pseudo-EPSC) driven firing patterns with increased cAMP

Next, we examined whether the enhanced activation of I_H yielded regular spiking. Although spontaneous spiking *in vivo* is driven

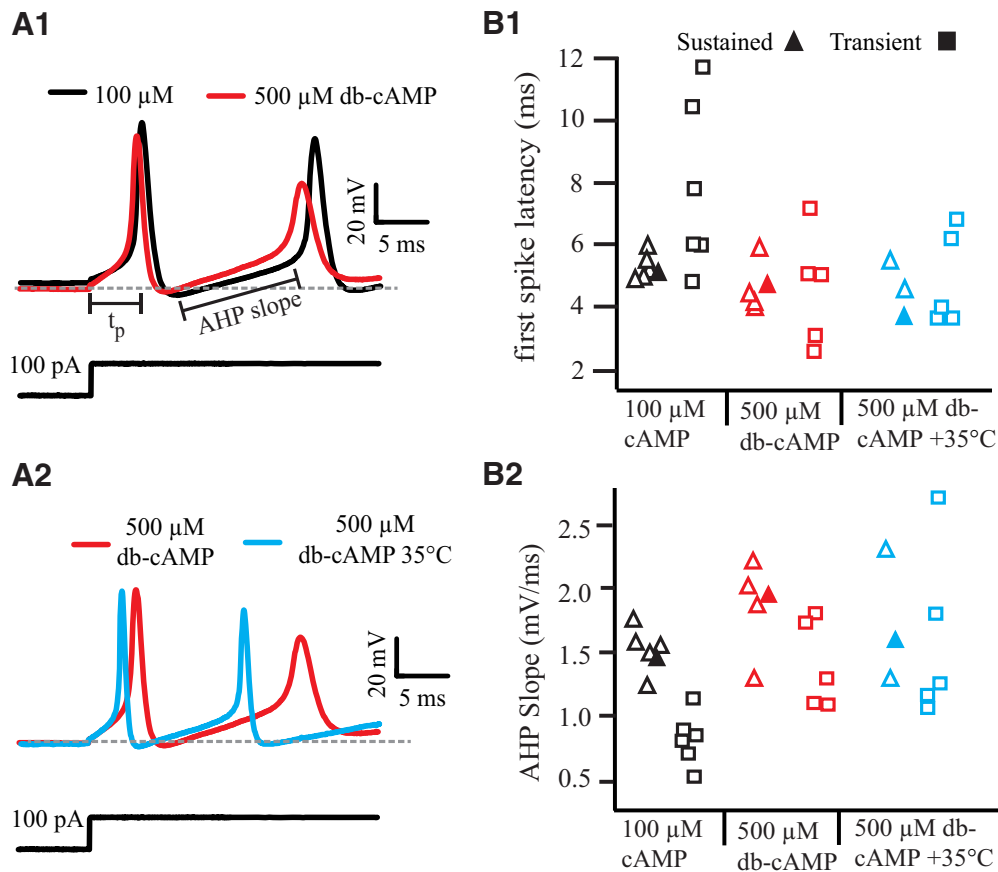


Figure 4. The effects of a db-cAMP and temperature on step-evoked firing patterns. **A1**, Example responses to a depolarizing current step for sustained-firing VGNs; one recording in 100 μM cAMP (black) and the second in 500 μM db-cAMP at 25°C (red) conditions. **A2**, Example responses to a depolarizing current step for sustained-firing VGNs; one recording in 500 μM db-cAMP at 25°C (red) condition and the second in 500 μM db-cAMP at 35°C (cyan) condition. VGN firing patterns in A were obtained in response to similar current step (~ 100 – 120 pA). First spike latency (t_p) and the slope of the afterhyperpolarization (AHP) trajectory were obtained as shown in **A1**. AHP slope was obtained by taking the slope of a line fit to the region illustrated in **A**. Dashed gray line shows -60 mV. **B1**, **B2**, Data for time to peak (ms) and AHP slope (mV/ms) for transient (\square) and sustained (Δ) is shown for all three conditions 100 μM cAMP (black $n = 11$) and 500 μM db-cAMP at both 25°C (red; $n = 10$) and 35°C (cyan; $n = 8$). Solid symbols are data for the example VGN shown in **A**.

by quantal release of neurotransmitter from hair-cells, dissociated VGNs require current injection to induce spiking. To mimic the random timing of synaptic input, we injected “pseudosynaptic” currents into VGN somata ($n = 47$; for additional detail see Materials and Methods; Kalluri et al., 2010). The size of the unitary EPSC was varied to drive neurons at different rates (Fig. 5A,B). Moreover, the average EPSC size needed to drive neurons to similar rates was larger in transient-firing neurons than sustained-firing neurons (Fig. 5C). Based on the steeper AHPs in step-evoked firing patterns, we hypothesized that firing rates should be higher in 500 μM db-cAMP where the enhanced activation of I_H contributed to the depolarization phase of spike generation. Recordings with 500 μM db-cAMP ($n = 11$) produced a mean firing rate of 30.4 ± 2.9 spikes/s, significantly higher than the 18.5 ± 1.0 spikes/s in the 10/100 μM condition ($p < 0.001$, Tukey HSD). However, when we looked at each condition by firing type we saw that this increase in mean firing rate was mainly driven by sustained-B-firing neurons ($n = 5$), which produced firing rates as high as 70 spikes/s in db-cAMP (Fig. 5C, black triangles). Again, increasing the temperature from 25°C to 35°C did not further increase mean firing rates beyond what was achieved with db-cAMP alone (32.6 ± 3.2 spikes/s, $n = 8$ vs 30.4 ± 2.9 spikes/s, $n = 11$).

Next, we quantified the regularity of spike timing with the CV of the ISI histograms (Fig. 5B). Smaller CV values correspond to

narrower histograms and more regularly-timed spike intervals. Figure 5D plots CV as a function of mean ISI measured for all cAMP conditions for ($n = 47$), of which eight were in 500 μM db-cAMP between 35°C and 37°C. Recall (from Materials and Methods) that we drove each cell to spike at different rates to allow us to compare CV across neurons at similar spike rates. Consequently, there are >47 points on the plot because each cell contributes more than one point.

We conducted a slope regression analysis to test the influence of ISI and cAMP condition on CV. Spike-train regularity was significantly dependent on ISI ($F_{(1,130)} = 7.015$, $p = 0.0092$) but not on cAMP condition ($F_{(4,130)} = 0.32$, $p = 0.8624$). In other words, this analysis suggests that once we account for the effect that increasing cAMP has on ISI (recall from Fig. 5C that cAMP condition does affect spike rate or the inverse of ISI), cAMP has no further influence on regularity. For example, even in 500 μM db-cAMP, were the activation range of I_H is most depolarized and ISIs were as short as 10 ms, firing patterns were still very irregular (with CV values > 0.45 ; Fig. 5D, blue triangles). This is counter to the findings in neonatal calyx terminals (Horwitz et al., 2014), where increasing cAMP or blocking I_H reduced CV by an order of magnitude (ranging from CV = 0.8–0.08).

Increasing the temperature from 25°C to 35°C in 500 μM db-cAMP did not significantly change mean firing rates (30.4 ± 2.9

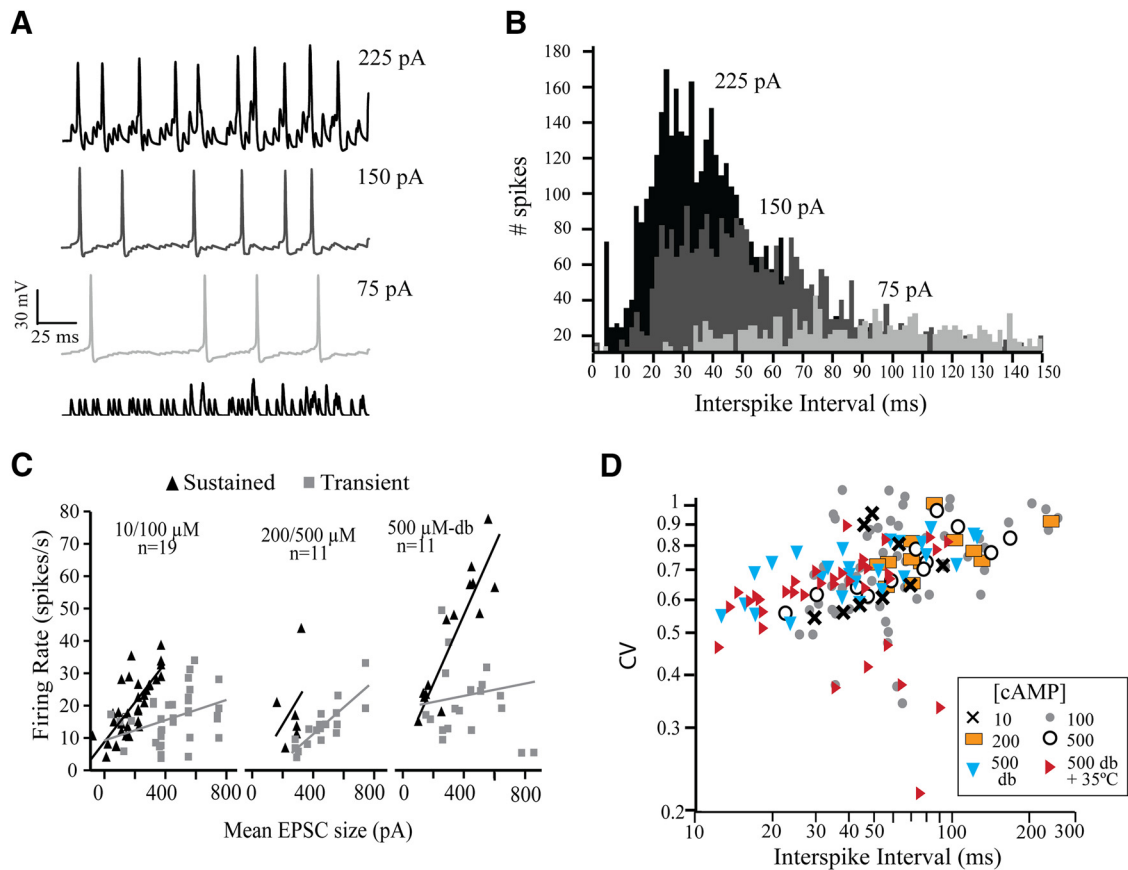


Figure 5. Enhancing I_H activation by increasing cAMP concentration does not increase spike-timing regularity. **A**, Spike trains in response to pseudo-synaptic current injection. Spike rate increased as the amplitude of unitary pseudo EPSC increased. **B**, ISI histograms constructed from spike trains in response to frozen variations of pseudo-synaptic currents. Mean spike interval (ISI) decreased as unitary EPSC amplitude increased compare black and gray histograms. **C**, Firing rate (spikes/s) as a function of mean EPSC amplitude (pA) in different cAMP concentrations. Mean firing rate was impacted by cAMP condition and mean EPSC amplitude. **D**, CV as a function of mean ISI (ms). Symbols represent cAMP conditions: 10 μM cAMP ($n = 4$; X), 100 μM cAMP ($n = 12$; gray \bullet), 200 μM cAMP ($n = 5$; orange rectangle), 500 μM cAMP ($n = 6$; black \circ), 500 μM db-cAMP ($n = 12$; blue ∇), and 500 μM db-cAMP at 35°C ($n = 8$; red \blacktriangleright). Forty-seven cells contributed to this plot, and an individual cell could have contributed multiple points.

spikes/s, $n = 11$ vs 32.6 ± 3.2 spikes/s, $n = 8$; $p = 0.56$). There is significant overlap between the red triangles and blue triangles in Figure 5D, except for a few spike trains with $\text{CV} < 0.5$ (which we discuss in the next section). These results suggest that regular spike trains do not emerge even with faster channel kinetics at higher temperature.

Overall, firing patterns were more irregular here than observed by Kalluri et al. (2010), who recorded from neonatal VGNs without explicitly controlling the activation of I_H . Thus, although activation of I_H via cAMP was sufficient to increase firing rates, it did not produce highly regular firing.

Developmental changes in firing patterns indicate acquisition of I_{KL}

An explanation for why VGNs failed to produce highly regular firing can be seen by examining the firing pattern of each cell in response to step currents. In Figure 6A, we recolored the symbols in Figure 5D according to step-evoked firing pattern. Triangles indicate recordings made between 35°C and 37°C. Transient-firing neurons (Fig. 6A) had the highest CV values (blue symbols), sustained-B firing neurons had intermediate CV values (gray symbols), and sustained-A firing neurons had the lowest CV values (red symbols). One sustained-A spiking neuron encountered in 500 μM db-cAMP at 35°C produced the most regular spike train in this study and was similar to that seen for sustained-A neurons by Kalluri et al. (2010) (Fig. 6A, red triangle

with $\text{CV} \sim 0.2$). This suggests that the firing pattern is the dominant predictor for spike-train regularity.

The above described firing-pattern-dependent stratification in CV is qualitatively consistent with that previously reported in younger VGNs (Kalluri et al., 2010) but is quantitatively very different. The overall range of CV values is much more compressed within the irregular/high CV region at the older ages in this study than at younger ages (shaded regions indicate the range of CVs reported by Kalluri et al., 2010). One striking difference between the two studies is that here we saw fewer cells that responded to current injections with sustained-A spike patterns, which appears to be a developmentally driven change. Figure 6B illustrates that the proportion of VGNs that fire with sustained-firing patterns diminishes during the first 3 postnatal weeks. During the first postnatal week, equal numbers of cells had either transient-firing or sustained-firing patterns (Fig. 6B); among the sustained-firing group $\sim 12\%$ had a fully sustained-A firing pattern. These proportions are very different by the third postnatal week when nearly 70% of cells had transient-firing patterns with very few cells having sustained-A firing patterns ($\sim 5\%$).

A shift toward the more phasic sustained-B-spiking and transient-spiking patterns is consistent with an increase in the expression of low-voltage-gated potassium currents (Iwasaki et al., 2008; Kalluri et al., 2010; Yoshimoto et al., 2015). Also, consistent with this suggestion, we found that there was an age-dependent hyperpolarization in resting potential (V_{rest}) and

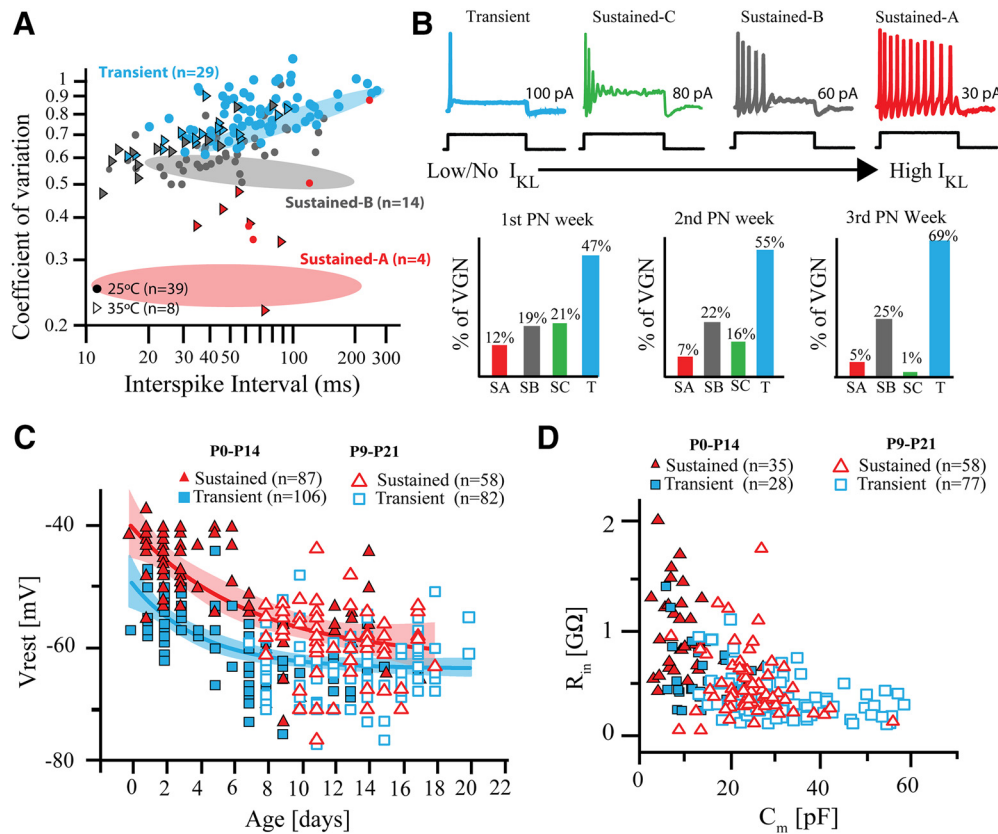


Figure 6. Age-dependent changes in firing pattern and passive membrane properties. **A**, The influence of firing-type on spike-timing regularity. Same data as in Figure 5D but separated by step-evoked firing pattern; transient-firing (blue; $n = 29$), sustained-B (gray; $n = 14$), and sustained-A (red; $n = 4$). Data obtained in 35°C are distinguished by the symbol \blacktriangleright ($n = 8$). Shaded regions represent the CV range reported by Kalluri et al. (2010) before the first 2 postnatal weeks. **B–D**, Data from the present study from more mature neurons (open symbols; $n = 130$) are pooled with that from the younger cells reported by Kalluri et al. (2010) (solid symbols; $n = 192$). **B**, Examples of VGN firing types in response to a 750 ms long current step. Bar plots showing the proportion of cells that fall into each firing-pattern group from the first, second, and third postnatal weeks. **C**, Resting potential becomes more negative with age for both firing types. During early postnatal days, the resting potential for sustained-firing cells (red triangles) were more depolarized than for transient-firing cells (blue squares). As indicated by the convergence of the two trend lines, this difference diminished at older ages. Trend lines are exponential fits to the pooled dataset with 95% confidence intervals (shaded regions) for transient (blue) and sustained (red) firing neurons. **D**, Input resistance (R_{in}) as a function of membrane capacitance (C_m), for 56 sustained and 71 transient neurons. On average, C_m is larger for older neurons, regardless of firing pattern. R_{in} becomes smaller for older sustained-spiking neurons. Together, **A–D** follow the idea that sustained-spiking cells are acquiring additional potassium currents as they mature.

decrease in input resistance (R_{in}) for all cell types. In Figure 6, **C** and **D**, we pooled data from the present study ($n = 146$) with those from Kalluri et al. (2010) ($n = 192$) to illustrate the age-dependent changes in these passive membrane properties. Resting potentials of sustained-spiking (red) and transient-spiking (blue) VGNs were different during early postnatal days but begin to converge with that of transient firing neurons by the third postnatal week (Fig. 6C). Membrane capacitance (C_m) was typically larger in the older dataset (Fig. 6D) with transient-firing neurons being larger (40.9 ± 1.4 pF, $n = 77$) than sustained-firing neurons (31.4 ± 1.7 pF, $n = 60$; $t_{(132,3)} = 4.45$, $p = 0.0001$, unpaired t test). When compared by cell size, R_{in} values were smaller in transient-firing neurons than sustained-firing neurons at younger ages (Fig. 6D, red triangles, blue squares), but the differences are less striking at older ages. These data suggest that the ion channel properties of VGNs are becoming less heterogeneous with development. This developmental shift in firing patterns likely accounts for why we did not see highly regular firing, despite enhancing the activation of I_H .

Modeling the influence of I_H activation in the presence and absence of I_{KL}

Our initial prediction was that by recording from older ages and increasing the activation of I_H we would have seen increased

sustained-A spiking in response to current steps and more regular spiking in response to pseudo-synaptic stimulation. However, on average, we saw the opposite result in that VGN responses shifted toward transient/irregular spiking. Next, we will show through model simulations that this result can be accounted for by considering the interaction between I_{KL} and I_H , both of which are present in nearly all VGNs at older ages.

We used a single-compartment conductance-based vestibular ganglion model in which we could control the conductance density of I_{KL} and the activation of I_H (see Materials and Methods; Hight and Kalluri, 2016). Sustained-A and sustained-B firing patterns were simulated (Fig. 7A1, B1) by setting g_{KL} to 0 and 0.65 (mS/cm²), respectively. The equations describing g_{KL} are the same as those described by Hight and Kalluri (2016) for currents carried through an equal combination of Kv1 and Kv7 type ion channels. Sodium channel density (g_{Na}) was set to 20 mS/cm² for all simulations. This value was large enough to avoid spike train adaptation because of sodium channel inactivation (Hight and Kalluri, 2016). A family of 1500 ms step depolarizing currents was used to elicit spike trains for each condition. Figure 7, A1 and B1, shows responses at current threshold. The conductance density for the HCN channel, g_H , was set from 0.07 through 0.91 mS/cm². This range is between 0.5 and 7 times the mean value we measured in VGNs (0.13 mS/cm²). Here we show the result for

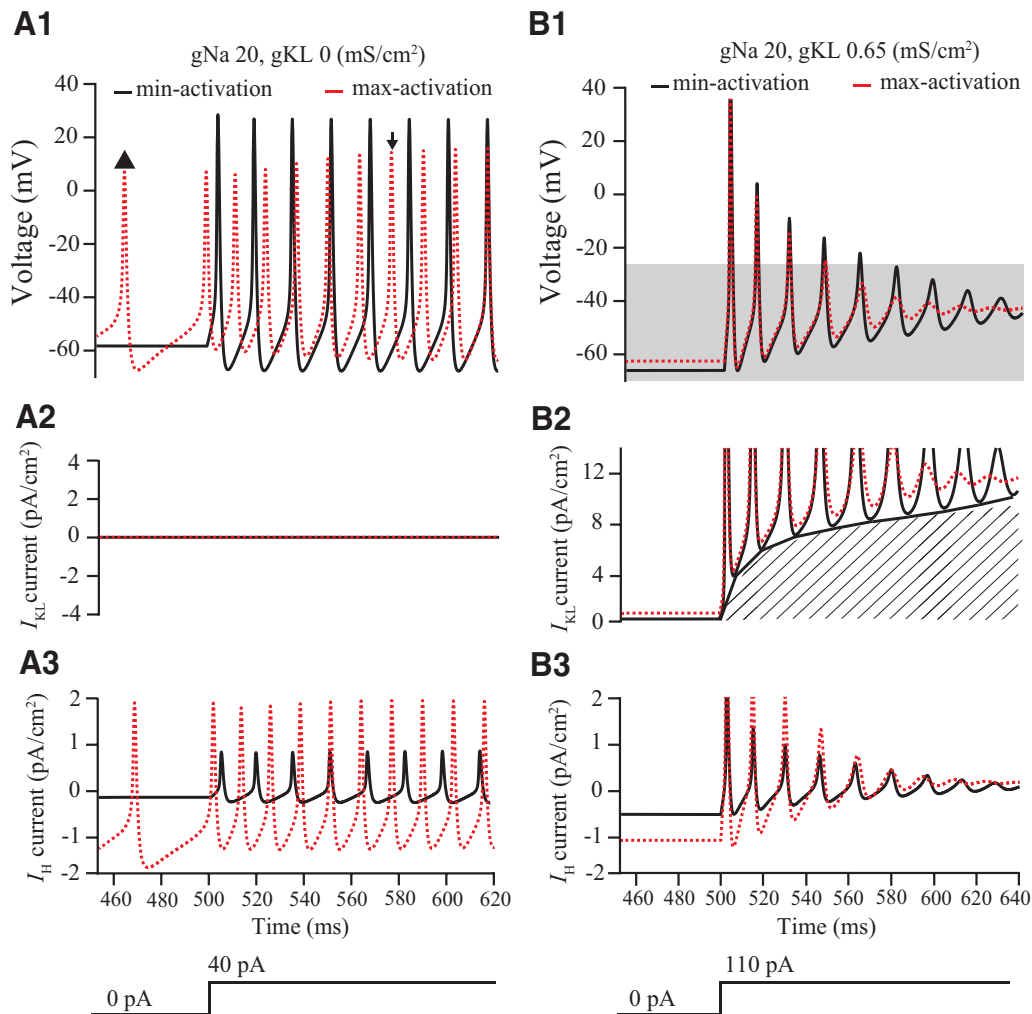


Figure 7. The influence of shifting the activation range of I_H explored in a conductance-based model. Model results from sustained-A and -B type VGNs in response to a 1500 ms depolarizing current step (**A3**, **B3**, bottom). Two I_H conditions are shown in each panel; minimum activation (black) and maximum activation (dashed red). **A**, **B**, The sustained-A type model was produced by setting g_{Na} to 20 mS/cm² and g_{KL} to 0. The sustained-B type model was produced by setting g_{Na} to 20 mS/cm² and g_{KL} to 0.65 mS/cm² composed equally of Kv1 and Kv7. **A1**, **B1**, Voltage-clamp responses for the sustained-A and -B models under model conditions for I_H current (minimum activation, where $V_{1/2} = -96$ mV and maximum activation, where $V_{1/2} = -84$ mV. Black triangle (\blacktriangle), The max activation produced spontaneous firing at rest. **B**, Sustained-B neurons exhibit accommodation as voltage oscillations are present in all I_H conditions after ~ 60 ms following the onset of the stimulus. **A2**, **B2**, I_{KL} current (pA/cm²) as a function of time for **A** and the shaded region in **B**. **A2**, No I_{KL} current is seen because g_{KL} is set to 0 for the sustained-A type VGN. **B2**, The I_{KL} current at rest and during the AHP grows larger as I_H is activated. Hatched region, To estimate the net charge (Q /cm²) carried by I_{KL} we took the sum of the area under each minimum, which is proportional to the shaded region. **A3**, **B3**, I_H current (pA/cm²) as a function of time for **A** and the shaded region in **B**. **A3–B3**, As expected the I_H current is larger at rest and throughout the stimulus for max activation cases than for the minimum-activation case. Note that because of the slow kinetics of the HCN channel, the current of I_H switches from inward (–) to outward (+) during the upswing of the spike.

the largest value because conductance density for I_H is reported to be larger in calyx terminals than in somata (Horwitz et al., 2014). We repeated simulations with two I_H conditions that represented the current's most hyperpolarized and depolarized voltage-dependent activation (minimum and maximum activation, representative of the 100 μ M cAMP and 500 μ M db-cAMP conditions, respectively). The parameters describing the voltage activation range and kinetics for these conditions were based on the data shown in Figure 3 and are represented by Equations 3–5 (see Materials and Methods; parameters are summarized in Table 1).

Activation of I_H excites faster spiking in the absence of I_{KL}

Figure 7A1–A3 shows the firing patterns and flow of currents through g_H and g_{KL} for the sustained-A simulation. Only the beginning of each spike train is shown to emphasize the details of spike shape and timing. Figure 7, A2 and A3, shows the flow of I_H and I_{KL} currents into and out of the cell (negative and positive

currents, respectively). When I_H was minimally activated, very little I_H current flows into the cell before current injection begins (i.e., the resting phase; Fig. 7A3). During current injection, the membrane potential depolarizes and the model produces spikes throughout the current step. Between each spike (as the cell emerges from the afterhyperpolarization), a little I_H current flows into the cell when the membrane potential is more negative than the reversal potential for I_H (-40 mV). When the membrane potential crosses the reversal potential, I_H current flows out of the cell. When the activation range of I_H is shifted in the maximum activation condition (dashed trace), there is significant I_H flowing into the cell during rest and between spikes. As a result of this extra depolarizing current, the model begins to spike spontaneously (Fig. 7A1, black triangles). The flow of inward and outward currents through the I_H conductance is also larger during the current injection resulting in shorter mean intervals between spikes (11.97 ± 0.12 vs 12.32 ± 0.01 ms) and more evoked spikes

during the step (139 vs 122 spikes). Also note that the spikes are much shorter in the maximum activation condition because the slow inactivation of I_H means that the channel remains open during the action potential, adding another large repolarizing potassium current past its reversal potential. Note that because of the spontaneous-spiking, the increase in spike rate during the current step is not immediately visible but, becomes more obvious by ~ 60 ms after stimulus onset (black arrow). Overall, the excitatory influence of I_H is consistent with the pace-making role of this current in cardiac cells (DiFrancesco, 2010) and with previous suggestions for vestibular afferents (Horwitz et al., 2014; Yoshimoto et al., 2015).

Activation of I_H dampens spiking in the presence of I_{KL}

The influence of I_H on firing patterns is different in the presence of I_{KL} . In Figure 7B1–B3, we show a simulated sustained-B firing-pattern by setting g_{KL} to 0.65 mS/cm². Again, the flow of I_{KL} and I_H currents during the simulation are shown under the firing pattern (Fig. 7B2,B3). As expected for a model containing I_{KL} there is some outward current flowing during the resting phase (Fig. 7B2). This translates to a more hyperpolarized resting potential for the sustained-B firing pattern (Fig. 7B) than for the sustained-A firing pattern (Fig. 7A). During current injection, the spike trains exhibited accommodation as the I_{KL} current prevented the simulation from reaching threshold, as evidenced by the loss of spikes and emergence of voltage oscillations in the later portions of the current step. In the maximum I_H activation condition, there was much more inward I_H current in the resting condition and a resulting depolarization in resting potential. However, this depolarization shifts the membrane potential further into the activation range for g_{KL} thereby also increasing the amount of outward flowing I_{KL} . The average outward flowing I_{KL} is larger in the maximum activation condition than in the minimum activation condition. This illustrates that activation of I_H recruited more I_{KL} both at rest and during spiking (Fig. 7B2). This recruitment results in spike trains accommodating faster in the maximum-activation condition than in the minimum-activation condition (Fig. 7B1). Thus, in the presence of I_{KL} , I_H has a net dampening effect on spiking.

The influence of I_H depends on I_{KL} density and channel composition

In Figure 7, we showed single examples in which I_H could both excite and dampen spiking, depending on the presence of I_{KL} . In further simulations we varied the size of g_{KL} from 0 to 0.8 mS/cm² (sustained-A through transient) while keeping all other conductance densities fixed to explore whether the effect on spiking depends on the relative densities of the two conductances. The composition of g_{KL} was comprised of one of the following: entirely Kv1 (Fig. 8, green), entirely Kv7 (blue), or equal proportions of the two conductances (magenta). We elicited spike trains using a fixed-length (1500 ms), fixed amplitude (55 pA), suprathreshold current step. Simulations were repeated in both the maximum (solid symbols) and minimum (open symbols) activation conditions for I_H to examine the influence of activating I_H . Figure 8A plots the number of spikes evoked by the current step as function of g_{KL} when comprised entirely by Kv1 type channels. As g_{KL} increases, the number of spikes evoked by the current step decreases. Beyond a threshold value, there is a dramatic transition, after which spike number drops precipitously with increasing g_{KL} . There are effectively two regimes to the response. First, there is a tonic regime where many spikes are evoked during the current injection and firing patterns are largely sustained-A. Sec-

ond, there is a phasic regime where firing patterns are sustained-B and transient.

Because g_{KL} can be comprised of different channel subtypes, we also examined the influence of channel composition by repeating the above simulations with 100% Kv7 or equal proportions of Kv1 and Kv7 (Fig. 8B). Recall that the Kv1 and Kv7 channel models have the same voltage-gated activation range but differ in that Kv1 activates quickly and experiences inactivation whereas the Kv7 activates slowly but does not inactivate (Eqs. 6,7). Regardless of channel composition, spike numbers decreased with increasing g_{KL} . However, the amount of g_{KL} needed to elicit the transition between the tonic and phasic regimes was much smaller when g_{KL} included Kv7 components. Also, spike number was more sensitive to increases in Kv7 than to increases in Kv1 (seen as a steeper slope in the spike number vs g_{KL} curve for the Kv7 and mixed conditions). These differences in the effective potency of Kv7 comes from the differences in the net steady-state current produced by the two models; because Kv7 does not inactivate, it produces more steady-state current than the Kv1 model, which experiences significant inactivation. Differences in the time course of activation also impacts firing pattern. Because Kv1 activates much more quickly than Kv7, the transition between the tonic and phasic regimes is much more abrupt for the Kv1 case. In contrast, for both the Kv7 and mixed Kv7/Kv1 conditions, the spike rate (proportional to total number of spikes) slows down substantially before the transition to the phasic regime.

When I_H is maximally activated, the influence of g_{KL} is enhanced, and the transition between the tonic and phasic regimes occurs at smaller g_{KL} values than in the minimum I_H condition (Fig. 8A,B, compare dashed lines to dotted lines within each g_{KL} condition). The influence of shifting the activation of I_H is very different in the regimes before and after the transition. In the tonic regime, the maximum activation condition produces more spikes than the minimum activation condition (i.e., the excitatory effect from the previous figure). However, as g_{KL} increases, the relative gain in spike numbers provided by I_H diminishes. After the transition, the maximum activation condition produces the opposite effect in that for any fixed value of g_{KL} , there is a decrease in the number of spikes evoked (i.e., the type of dampening seen in Fig. 7B). Together, these results show that the outward flowing potassium currents carried by g_{KL} counteract the excitatory influence of I_H . Moreover, more g_{KL} is recruited when the activation range of I_H is depolarized toward the activation range of g_{KL} .

To examine the influence of I_H in isolation from the complexities of g_{KL} recruitment and kinetics, we plotted the spike number and the regularity of the spike train as a function of Q_{KL} , the net subthreshold charge delivered by g_{KL} (Fig. 8C,D, respectively). We computed Q_{KL} as the area under the lower envelop of the I_{KL} versus time curve (Fig. 7B2, hatched area). Note that this is not the same as the net charge delivered by g_{KL} during the entire spike train, but rather an estimate of the current during the subthreshold portions of the spike-train. As expected, spike number decreases as Q_{KL} increases. Now, however spike number falls along a single curve rather than three parametric curves for each combination of Kv1/Kv7. In this plot, we see that the influence of I_H alone (when isolated from its ability to recruit I_{KL}) is excitatory in that it produces more spikes. This is true in both the tonic and phasic regimes (compare open symbols to closed symbols).

To examine the influence of I_H on spike-timing regularity in the simulations, we computed the CV values for the step-evoked spike trains that produced >10 spikes (Fig. 8D); meaning that regularity was only computed within the tonic regime. We make three main observations pertaining to CV. First, all CV values were highly reg-

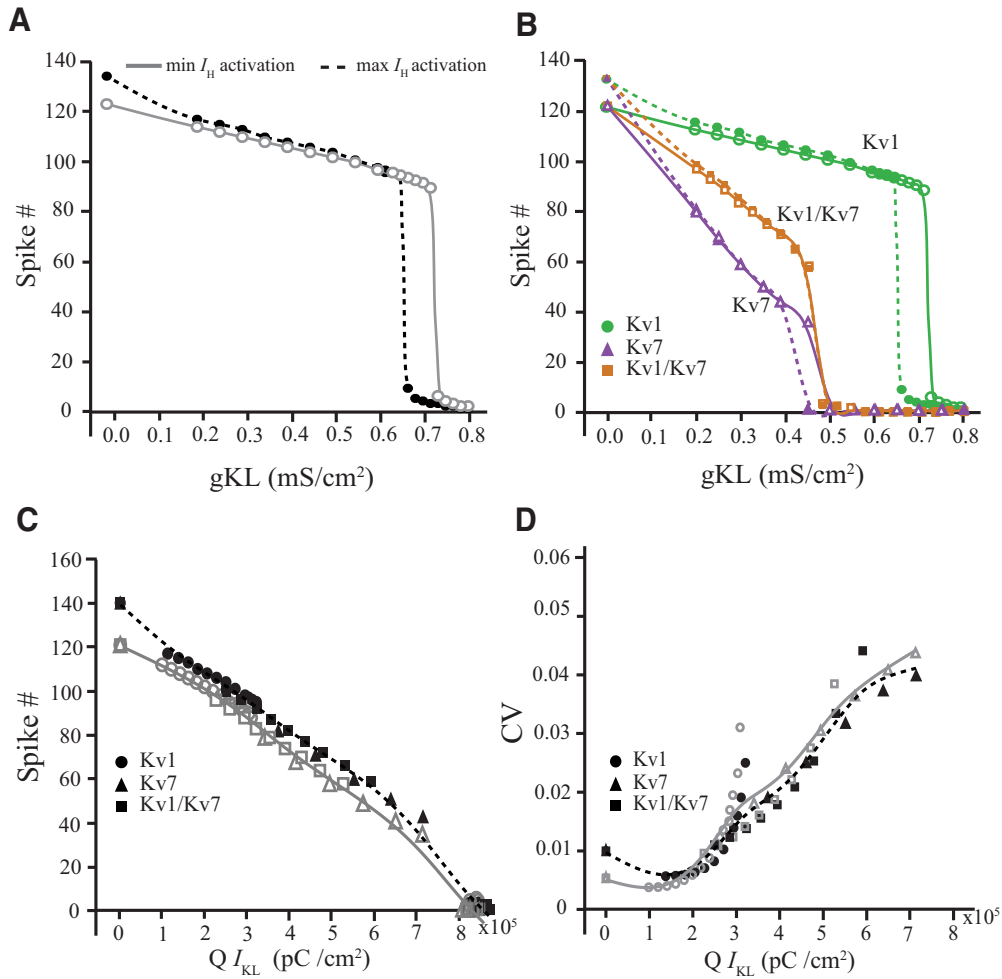


Figure 8. I_{KL} is the dominant influence on spike number and spike timing. Model VGN with g_{KL} values between 0.0 and 0.8 mS/cm², Kv1 to Kv7 ratios for I_{KL} of 1.0 Kv1 (green, ● or ○), 50% Kv1 and Kv7 (magenta, ■ or □), or 1.0 Kv7 (blue, ▲ or △) were driven with a 1500 ms depolarizing current step (55 pA). Each model VGN had either minimum (open symbols) and maximum I_H (solid symbols) I_H activation. Trend curves through the data are shown as solid or dashed lines, respectively. **A**, Only spikes during the current step were used to compute spike number. Spike number as a function of g_{KL} (1.0 Kv1) for min and max I_H activation. Spike number falls as g_{KL} increases and drops sharply once a large enough g_{KL} is reached and because of rapid adaption of the spike train (data not shown). Max activation of I_H provides a modest boost in spike number over min activation but requires a smaller g_{KL} value to illicit adaption. **B**, Spike number as a function of g_{KL} for three model VGNs with I_{KL} ratios of 1.0 Kv1, Kv1/Kv7, and 1.0 Kv7. For all three model VGNs, spike number falls as g_{KL} increases and drops sharply once a large enough g_{KL} is reached and adaption occurs. This g_{KL} value is smallest in 1.0 Kv7 and largest in 1.0 Kv1 model VGNs. Max activation of I_H condition requires a smaller g_{KL} value to elicit accommodation for both the 1.0 Kv1 and 1.0Kv7 model VGNs. **C**, Spike number as a function of net charge carried by I_{KL} ($Q I_{KL}$, pC/cm²). Activation of I_H provides a modest increase in spike number regardless of net charge by I_{KL} or composition of I_{KL} . **D**, CV as a function of net charge carried by I_{KL} for model VGNs that produced at least 10 spikes. CV increased as net charge by I_{KL} increased. CV values overall were highly regular (CV < 0.05) because of the lack of irregularity imposed by the step stimulus.

ular (CV 0.005–0.05). We attributed this to the stimulus type, compared with the randomly arriving EPSC trains, steps of current impose relatively little irregularity onto the sustained-A model. Second, overall CV increased with Q_{KL} . Because the transition from the tonic to phasic regime was most abrupt for the Kv1 dominated g_{KL} (Fig. 8B), the change in regularity was also most abrupt for this channel composition (Fig. 8D, compare green symbols to blue + magenta). Third, activation of I_H produced only modest changes in CV between 2 and 8 pC/cm² (Fig. 8D, compare solid and dashed trend lines). Spike-timing regularity is much more sensitive to variations in low-voltage-gated potassium currents than to I_H . In other words, highly-regular spiking could not be produced by simply increasing I_H , but only occurred with small Q_{KL} . Interestingly, CV depends on Q_{KL} non-monotonically, with a small upturn toward higher CV values at the lowest Q_{KL} . In this regime, the step-evoked spike trains are non-adapting with spikes arriving with clock-like precision. Because CV is the ratio of the SD to the mean of spike intervals, the decrease in mean intervals combined with invariance

in the SD produces the increase in CV. Similarly, maximizing I_H within this regime produces faster spiking but also produces higher CVs.

Discussion

A developmental convergence in VGN firing patterns

Here we considered whether highly-regular spiking relies on HCN channels, known to be present in both VGN and calyx terminals (Almanza et al., 2012; Meredith et al., 2012; Horwitz et al., 2014; Yoshimoto et al., 2015). We recorded firing patterns from VGNs after expression for HCN channels is developmentally upregulated (Almanza et al., 2012; Yoshimoto et al., 2015) and we enhanced the activation of HCN-mediated currents (referred to as I_H in the text) by increasing intracellular concentrations of cyclic-AMP (Accili et al., 2002; Almanza et al., 2012; Meredith et al., 2012). With HCN-mediated currents so enhanced, we found faster subthreshold depolarizations and faster firing rates, but did not find more regular spiking. A concomitant

developmental increase in low-voltage-gated potassium currents (referred to as I_{KL} in the text) likely countered the influence of HCN-mediated currents to prevent highly-regular spiking.

Ample evidence supports the idea that low-voltage-gated potassium currents grow with development. Patch-clamp recordings in VGNs show that the currents are larger in the second postnatal week than in the first (Kalluri et al., 2010). Consistent with this, we found resting potentials hyperpolarized and input resistance decreased with age. Overall, VGN responses became less diverse, converging toward more phasic and irregular firing patterns.

Developmental upregulation in the Kv7 group of low-voltage-gated potassium channels (also known as KCNQ channels) is likely driving this change. Immunohistochemistry and pharmacology showing expression for and regional upregulation of Kv7 channels support this conjecture (Rennie and Streeter, 2006; Pérez et al., 2009; Kalluri et al., 2010; Meredith and Rennie, 2015). Immunolabeling for Kv7 channels is initially confined to neurons innervating the central/striolar zones of the vestibular sensory epithelia and eventually spreads to the peripheral/extrastriolar zones (Hurley et al., 2006). As a consequence, calyx terminals in the peripheral zones have little low-voltage-gated potassium currents during early postnatal days (Songer and Eatock, 2013) but have significant increase in these currents mediated by the second to third postnatal weeks (in gerbils, Meredith and Rennie, 2015; in mice, Ramirez et al., 2018; based on sensitivity to Kv7-specific antagonists, linopiridine or XE991). By P21, nearly all VGNs in mice immunolabel for Kv7 (Rocha-Sanchez et al., 2007). Consistent with this, conversion from transient to sustained spiking can require blocking of both Kv1- and Kv7-mediated low-voltage-gated potassium currents (Kalluri et al., 2010). Together, these results suggest that most vestibular afferents eventually acquire low-voltage-gated potassium currents, driven, in part, by a developmental upregulation in Kv7 channels.

Comparison to previous studies

Iwasaki et al. (2008) described a different developmental trajectory in which a larger fraction of VGNs had tonic/sustained firing patterns as function of development. They interpret this as reflecting an age-dependent increase in HCN channel expression (Yoshimoto et al., 2015) coupled with a relatively age-invariant dependence for Kv1 expression (Iwasaki et al., 2012). This trajectory is satisfying because it describes a pattern of ion channel expression that parallels the *in vivo* increase in regular-spiking (Curthoys, 1979). However, unlike the present study and those of Soto and colleagues (Limón et al., 2005; Pérez et al., 2009; Almanza et al., 2012), Yoshimoto et al. (2015) recorded from small cells whose size, resting potentials and input resistance did not change with age. Their cells also lacked Kv7-mediated currents because they could convert firing patterns from transient to sustained-firing by only blocking Kv1 channels (Iwasaki et al., 2012). In contrast, we saw a wide range of cell sizes, age-dependent hyperpolarization in resting potential and, in a previous study, showed that it is necessary to block both Kv1 and Kv7 channels to convert firing patterns (Kalluri et al., 2010). Whether or not methodological variations, including differences in enzyme composition and maturational sensitivity to enzymes leads to sampling different subpopulation and/or alters ion channel properties remains to be resolved (Quandt, 1987; Matteson and Carmeliet, 1988; Armstrong and Roberts, 1998).

Horwitz et al. (2014) showed impressive control over spike-timing regularity by blocking or enhancing HCN-mediated cur-

rents in the calyx terminals of immature dimorphic afferents. This is likely because immature calyces do not yet have their full complement of potassium currents. Our modeling suggests that the absence of low-voltage-gated potassium currents in immature calyces created the ideal condition for HCN-mediated currents to influence spike-timing regularity. Indeed, Songer and Eatock (2013) found sustained spiking and highly regular spontaneous spiking in early postnatal extrastriolar calyces, indicating that these neurons lacked low-voltage-gated potassium currents. In contrast, striolar calyces have these currents and respond to injected currents with transient/phasic spiking and spontaneously spike with irregular timing. We also considered whether HCN-mediated currents could exert a stronger influence on spike timing at calyx terminals where the current's densities are larger than they are at somata (Horwitz et al., 2014). Our modeling argues against this line of reasoning because even with seven times the HCN channel density found in the somata, the size of low-voltage-gated potassium currents was still the dominant factor controlling spike timing. These results suggest that differences in the size of HCN-mediated currents between terminals and somata do not account for the prevalence of phasic and irregular firing in the present study.

Ion channel mechanisms controlling spike-timing

HCN-channels are permeable to both sodium and potassium ions, which gives them a reversal potential ~ -40 mV (which is near spike threshold in VGN; DiFrancesco, 1981; present study). At subthreshold potentials, current flows into the cell through HCN channels. This steady inward current depolarizes the membrane potential toward spike threshold driving highly-regular auto-rhythmic firing (DiFrancesco, 2010; Horwitz et al., 2014). This follows our observations in $500 \mu\text{M}$ db-cAMP, where we found steeper afterhyperpolarization potentials and faster spike rates that are akin to those seen *in vivo* (Fig. 4). This role of HCN-mediated currents in shaping the afterhyperpolarization potential is similar in spirit (if not in the details) to the phenomenological “afterhyperpolarization current” model for explaining spike-timing regularity in vestibular neurons (Smith and Goldberg, 1986). Because HCN channels inactivate slowly, the resulting steady inward current can raise resting potential and increase net conductance, simultaneously sharpening excitatory postsynaptic potentials and speeding action potential timing (in the auditory nerve, Yi et al., 2010; in the vestibular nerve, Meredith et al., 2012).

HCN-mediated currents influence spiking very differently when they are found with low-voltage-gated potassium currents. As the inward flowing HCN-mediated current depolarizes a neuron, the membrane potential comes closer into the activation range of low-voltage-gated potassium channels. When these potassium channels open, the net outward current works against the HCN-mediated inward current to pull the membrane potential away from spike threshold, making it harder for the neuron to reach spike threshold. How quickly spiking is inhibited depends on the type of low-voltage-gated potassium channel. Fast-activating currents from Kv1 channels quickly tamp-down spiking, whereas the slower activating currents mediated by Kv7 channels often allow several spikes to trigger before the outward current is large enough to squelch spiking (Fig. 7).

The interactions between multiple ion channels determine neuronal excitability, which is a general feature of neuronal biophysics. The role of any particular channel is greatly influenced by the complement of other channels found within neurons' membrane. In early development, HCN channels in vestibular afferents can be ex-

citatory and drive auto-rhythmic spiking, but, their role flips with the maturational upregulation of potassium channels. This interaction between HCN-mediated and low-voltage-gated potassium currents is similar to that described in the auditory brainstem (Bal and Oertel, 2000; Rothman and Manis, 2003; McGinley and Oertel, 2006; Mathews et al., 2010; Cao and Oertel, 2011; Khurana et al., 2012), where HCN-mediated currents enhance the inhibitory influence of low-voltage-gated potassium currents. These results suggest that although HCN-mediated currents grow during maturation, they counter-intuitively suppress VGN excitability by recruiting larger low-voltage-gated potassium currents. This drives maturing VGNs *in vitro* toward phasic and irregular spike-timing statistics.

If low-voltage-gated potassium currents are ubiquitously upregulated in vestibular afferents, then existing models accounting for spiking-timing regularity need revision. Our results argue against the hypothesis that developmental upregulation in HCN channel expression is responsible for developmental increases in regular-spiking *in vivo*. The ion channel complement controlling spike-timing is becoming more complex during maturation. Added complexity comes with added flexibility. In maturing VGN, low-voltage-gated potassium currents are driven through by both Kv1 and Kv7 channels. The Kv7-mediated currents can be modulated by cholinergic efferent neurons acting on muscarinic acetylcholine receptors. Muscarinic acetylcholine receptors are a G-protein-coupled receptors that trigger secondary-messenger cascades that ultimately close Kv7 channels (Selyanko et al., 1992; Selyanko and Brown, 1993; for review, see Brown, 2010; for review, see Greene and Hoshi, 2017).

Closing Kv7 channels in VGNs (either directly by blocking the channels or indirectly using the mAChR agonist oxotremorine-M) decreases membrane conductance, converts *in vitro* firing patterns from high-threshold transient-firing to low-threshold sustained-firing (Pérez et al., 2009) and increases the regularity of spontaneous firing in extra-striolar calyces (Ramirez et al., 2018). Consistent with this, turtle vestibular efferent neurons close Kv7 channels to excite a slow increase of *in vivo* afferent spike rate (Holt et al., 2017). Similarly, blocking Kv7 channels suppresses *in vivo* afferent response to transient head motions in mice (likely encoded by irregular afferents; Lee et al., 2017). This suggests that maturing vestibular afferents acquire ion channel properties than can be dynamically controlled, with some neurons possibly acquiring the flexibility to move between the regular- and irregular-firing categories, perhaps based on the tone established by descending efferent projections. This is interesting for neurons outside the vestibular system that also require control over their spike timing and suggests one way in which this level of dynamic control can be achieved.

Our results also suggest that temperature differences (e.g., room temperature vs body temperature) do not significantly account for the differences in spike-timing regularity between *in vitro* and *in vivo* experiments. We previously found that increasing recording temperature speeds up ion channel kinetics and spike rates (present study; Kalluri et al., 2010). Similarly, spike rates are nearly six times faster at body temperature than room temperature in auditory nerve (Wu et al., 2016). Surprisingly, here we found that *in vitro* spike-timing for VGNs is neither faster nor more regular at body temperature than at room temperature when cAMP levels are already elevated ($CV > 0.5$ in both cases). At first blush, this seems surprising because increasing body temperature speeds up ion channel kinetics (shown here for HCN channels in VGNs) and is

known to depolarize the voltage activation range of HCN channels (Gambardella et al., 2012). However, as our experiments show the combination of elevated cAMP concentrations and elevated temperature are not enough to unveil the highly regular spiking found *in vivo* ($CV < 0.1$; Baird et al., 1988). This supports our primary conclusion that highly regular-spiking in vestibular ganglion neurons is limited by the presence of low-voltage-gated potassium channels and not by the size, speed, and activation state of HCN channels.

Ultimately, the ion channel mechanisms we describe *in vitro* represent only a piece of the puzzle contributing to *in vivo* responses. Vestibular afferents have diverse dendritic morphologies, connect to different types and numbers of hair cells in different epithelial zones, and express a variety of ion channels (many were not considered here). In addition to ion channels, models have shown that the size and rate of synaptic events also shapes spike-timing statistics. For example, turtle vestibular neurons having small compact terminal arbors with bouton synapses on few hair cells might produce large and temporally brief synaptic events whereas neurons with extended arbors containing hundreds of bouton-like terminals on many spatially dispersed hair cells may produce small but rapidly arriving events (Goldberg and Holt, 2013; Holmes et al., 2017). A sustained-A model can produce remarkably regular firing patterns when stimulated by a steady depolarization, such as that provided by a step of current (Fig. 8) or by the convergence of small but rapidly arriving synaptic events (Hight and Kalluri, 2016). Consistent with this, regular-firing dimorphic afferents in the peripheral zones of canal afferents appear to have more bouton terminals than those in the central zones (Goldberg et al., 1990b). A similar stimulus with small events arriving at high-rate applied to the transient-spiking model cannot even produce a spike train (Hight and Kalluri, 2016). In the future, we will need to consider whether ion channel composition (including efferent modulation) and terminal morphology/connectivity are complimentary specializations, tuned together over development to produce regular and irregular firing patterns.

References

- Accili EA, Proenza C, Baruscotti M, DiFrancesco D (2002) From funny current to HCN channels: 20 years of excitement. *News Physiol Sci* 17:32–37.
- Almanza A, Luis E, Mercado F, Vega R, Soto E (2012) Molecular identity, ontogeny, and cAMP modulation of the hyperpolarization-activated current in vestibular ganglion neurons. *J Neurophysiol* 108:2264–2275.
- Angelo K, Margrie TW (2011) Population diversity and function of hyperpolarization-activated current in olfactory bulb mitral cells. *Sci Rep* 1:50.
- Armstrong CE, Roberts WM (1998) Electrical properties of frog saccular hair cells: distortion by enzymatic dissociation. *J Neurosci* 18:2962–2973.
- Baird RA, Desmadryl G, Fernández C, Goldberg JM (1988) The vestibular nerve of the chinchilla: II. Relation between afferent response properties and peripheral innervation patterns in the semicircular canals. *J Neurophysiol* 60:182–203.
- Bal R, Oertel D (2000) Hyperpolarization-activated, mixed-cation current (I_h) in octopus cells of the mammalian cochlear nucleus. *J Neurophysiol* 84:806–817.
- Barry PH (1994) JPCalc, a software package for calculating liquid junction potential corrections in patch-clamp, intracellular, epithelial and bilayer measurements and for correcting junction potential measurements. *J Neurosci Methods* 51:107–116.
- Biel M, Wahl-Schott C, Michalakis S, Zong X (2009) Hyperpolarization-activated cation channels: from genes to function. *Physiol Rev* 89:847–885.
- Bond CT, Pessia M, Xia XM, Lagrutta A, Kavanaugh MP, Adelman JP (1994) Cloning and expression of a family of inward rectifier potassium channels. *Receptors Channels* 2:183–191.

- Brown DA (2010) Muscarinic acetylcholine receptors (mAChRs) in the nervous system: some functions and mechanisms. *J Mol Neurosci* 41:340–346.
- Brown HF, DiFrancesco D, Noble SJ (1979) How does adrenaline accelerate the heart? *Nature* 280:235–236.
- Campos-Toimil M, Keravis T, Orallo F, Takeda K, Lugnier C (2008) Short-term or long-term treatments with a phosphodiesterase-4 (PDE4) inhibitor result in opposing agonist-induced Ca^{2+} responses in endothelial cells. *Br J Pharmacol* 154:82–92.
- Cao XJ, Oertel D (2011) The magnitudes of hyperpolarization-activated and low-voltage-activated potassium currents co-vary in neurons of the ventral cochlear nucleus. *J Neurophysiol* 106:630–640.
- Chabbert C, Chambard JM, Valmier J, Sans A, Desmadryl G (2001) Hyperpolarization-activated (I_h) current in mouse vestibular primary neurons. *Neuroreport* 12:2701–2704.
- Curthoys IS (1979) The development of function of horizontal semicircular canal primary neurons in the rat. *Brain Res* 167:41–52.
- Desmadryl G, Chambard JM, Valmier J, Sans A (1997) Multiple voltage-dependent calcium currents in acutely isolated mouse vestibular neurons. *Neuroscience* 78:511–522.
- DiFrancesco D (1981) A study of the ionic nature of the pace-maker current in calf Purkinje fibres. *J Physiol* 314:377–393.
- DiFrancesco D (2010) The role of the funny current in pacemaker activity. *Circ Res* 106:434–446.
- Felix R, Sandoval A, Sánchez D, Gómora JC, De la Vega-Beltrán JL, Treviño CL, Darszon A (2003) ZD7288 inhibits low-threshold Ca^{2+} channel activity and regulates sperm function. *Biochem Biophys Res Commun* 311:187–192.
- Fernández C, Baird RA, Goldberg JM (1988) The vestibular nerve of the chinchilla: I. Peripheral innervation patterns in the horizontal and superior semicircular canals. *J Neurophysiol* 60:167–181.
- Fernández C, Goldberg JM, Baird RA (1990) The vestibular nerve of the chinchilla: III. Peripheral innervation patterns in the utricular macula. *J Neurophysiol* 63:767–780.
- Gambardella C, Pignatelli A, Belluzzi O (2012) The h-current in the substantia nigra pars compacta neurons: a re-examination. *PLoS One* 7:e52329.
- Goldberg JM (2000) Afferent diversity and the organization of central vestibular pathways. *Exp Brain Res* 130:277–297.
- Goldberg JM, Holt JC (2013) Discharge regularity in the turtle posterior crista: comparisons between experiment and theory. *J Neurophysiol* 110:2830–2848.
- Goldberg JM, Desmadryl G, Baird RA, Fernández C (1990a) The vestibular nerve of the chinchilla: IV. Discharge Properties of Utriclar Afferents. *J Neurophysiol* 63:781–790.
- Goldberg JM, Desmadryl G, Baird RA, Fernández C (1990b) The vestibular nerve of the chinchilla: V. Relation between afferent discharge properties and peripheral innervation patterns in the utricular macula. *J Neurophysiol* 63:791–804.
- Greene DL, Hoshi N (2017) Modulation of Kv7 channels and excitability in the brain. *Cell Mol Life Sci* 74:495–508.
- Highstein SM, Politoff AL (1978) Relation of interspike baseline activity to the spontaneous discharges of primary afferents from the labyrinth of the toadfish, *Opsanus tau*. *Brain Res* 150:182–187.
- Hight AE, Kalluri R (2016) A biophysical model examining the role of low-voltage-activated potassium currents in shaping the responses of vestibular ganglion neurons. *J Neurophysiol* 116:503–521.
- Holmes WR, Huwe JA, Williams B, Rowe MH, Peterson EH (2017) Models of utricular bouton afferents: role of afferent-hair cell connectivity in determining spike train regularity. *J Neurophysiol* 117:1969–1986.
- Holt JC, Jordan PM, Lysakowski A, Shah A, Barsz K, Contini D (2017) Muscarinic acetylcholine receptors and M-currents underlie efferent-mediated slow excitation in calyx-bearing vestibular afferents. *J Neurosci* 37:1873–1887.
- Horwitz GC, Risner-Janiczek JR, Holt JR (2014) Mechanotransduction and hyperpolarization-activated currents contribute to spontaneous activity in mouse vestibular ganglion neurons. *J Gen Physiol* 143:481–497.
- Hurley KM, Gaboyard S, Zhong M, Price SD, Wooltorton JR, Lysakowski A, Eatock RA (2006) M-like K^+ currents in type I hair cells and calyx afferent endings of the developing rat utricle. *J Neurosci* 26:10253–10269.
- Iwasaki S, Chihara Y, Komuta Y, Ito K, Sahara Y (2008) Low-voltage-activated potassium channels underlie the regulation of intrinsic firing properties of rat vestibular ganglion cells. *J Neurophysiol* 100:2192–2204.
- Iwasaki S, Nakajima T, Chihara Y, Inoue A, Fujimoto C, Yamasoba T (2012) Developmental changes in the expression of Kv1 potassium channels in rat vestibular ganglion cells. *Brain Res* 1429:29–35.
- Kalluri R, Xue J, Eatock RA (2010) Ion channels set spike timing regularity of mammalian vestibular afferent neurons. *J Neurophysiol* 104:2034–2051.
- Khurana S, Liu Z, Lewis AS, Rosa K, Chetkovich D, Golding NL (2012) An essential role for modulation of hyperpolarization-activated current in the development of binaural temporal precision. *J Neurosci* 32:2814–2823.
- Lee C, Holt JC, Jones TA (2017) Effect of M-current modulation on mammalian vestibular responses to transient head motion. *J Neurophysiol* 118:2991–3006.
- Limón A, Pérez C, Vega R, Soto E (2005) Ca^{2+} -activated K^+ -current density is correlated with soma size in rat vestibular-afferent neurons in culture. *J Neurophysiol* 94:3751–3761.
- Liu Q, Manis PB, Davis RL (2014) I_h and HCN channels in murine spiral ganglion neurons: tonotopic variation, local heterogeneity, and kinetic model. *J Assoc Res Otolaryngol* 15:585–599.
- Lysakowski A, Gaboyard-Niay S, Calin-Jageman I, Chatlani S, Price SD, Eatock RA (2011) Molecular microdomains in a sensory terminal, the vestibular calyx ending. *J Neurosci* 31:10101–10114.
- Mathews PJ, Jercog PE, Rinzel J, Scott LL, Golding NL (2010) Control of submillisecond synaptic timing in binaural coincidence detectors by K_1 channels. *Nat Neurosci* 13:601–609.
- Matteson DR, Carmeliet P (1988) Modification of K channel inactivation by papain and *N*-bromoacetamide. *Biophys J* 53:641–645.
- McGinley MJ, Oertel D (2006) Rate thresholds determine the precision of temporal integration in principal cells of the ventral cochlear nucleus. *Hear Res* 216–217:52–63.
- Meredith FL, Rennie KJ (2015) Zonal variations in K^+ currents in vestibular crista calyx terminals. *J Neurophysiol* 113:264–276.
- Meredith FL, Benke TA, Rennie KJ (2012) Hyperpolarization-activated current (I_h) in vestibular calyx terminals: characterization and role in shaping postsynaptic events. *J Assoc Res Otolaryngol* 13:745–758.
- Pérez C, Limón A, Vega R, Soto E (2009) The muscarinic inhibition of the potassium M-current modulates the action-potential discharge in the vestibular primary-afferent neurons of the rat. *Neuroscience* 158:1662–1674.
- Quandt FN (1987) Burst kinetics of sodium channels which lack fast inactivation in mouse neuroblastoma cells. *J Physiol* 392:563–585.
- Ramírez OL, Garrido AG, Koizumi K, Lysakowski A, Eatock RA (2018) KV channels, synaptic transmission and spiking in afferent terminals of the mouse utricular epithelium. 41st Annual Midwinter Meeting for the Association for Research in Otolaryngology. Abs # Sym30, San Diego.
- Rennie KJ, Streeter MA (2006) Voltage-dependent currents in isolated vestibular afferent calyx terminals. *J Neurophysiol* 95:26–32.
- Risner JR, Holt JR (2006) Heterogeneous potassium conductances contribute to the diverse firing properties of postnatal mouse vestibular ganglion neurons. *J Neurophysiol* 96:2364–2376.
- Rocha-Sanchez SM, Morris KA, Kachar B, Nichols D, Fritzsche B, Beisel KW (2007) Developmental expression of Kcnq4 in vestibular neurons and neurosensory epithelia. *Brain Res* 1139:117–125.
- Rothman JS, Manis PB (2003) The roles potassium currents play in regulating the electrical activity of ventral cochlear nucleus neurons. *J Neurophysiol* 89:3097–3113.
- Sadeghi SG, Chacron MJ, Taylor MC, Cullen KE (2007) Neural variability, detection thresholds, and information transmission in the vestibular system. *J Neurosci* 27:771–781.
- Sánchez-Alonso JL, Halliwell JV, Colino A (2008) ZD 7288 inhibits T-type calcium current in rat hippocampal pyramidal cells. *Neurosci Lett* 439:275–280.
- Schessel DA, Ginzberg R, Highstein SM (1991) Morphophysiology of synaptic transmission between type I hair cells and vestibular primary afferents: an intracellular study employing horseradish peroxidase in the lizard, *calotes versicolor*. *Brain Res* 544:1–16.
- Selyanko AA, Brown DA (1993) Effects of membrane potential and muscarine on potassium M-channel kinetics in rat sympathetic neurones. *J Physiol* 472:711–724.
- Selyanko AA, Stansfeld CE, Brown DA (1992) Closure of potassium

- M-channels by muscarinic acetylcholine-receptor stimulants requires a diffusible messenger. *Proc Biol Sci* 250:119–125.
- Smith CE, Goldberg JM (1986) A stochastic afterhyperpolarization model of repetitive activity in vestibular afferents. *Biol Cybern* 54:41–51.
- Songer JE, Eatock RA (2013) Tuning and timing in mammalian type I hair cells and calyceal synapses. *J Neurosci* 33:3706–3724.
- Takumi T, Ishii T, Horio Y, Morishige K, Takahashi N, Yamada M, Yamashita T, Kiyama H, Sohmiya K, Nakanishi S, Kurachi Y (1995) A novel ATP-dependent inward rectifier potassium channel expressed predominantly in glial cells. *J Biol Chem* 270:16339–16346.
- Wu JS, Young ED, Glowatzki E (2016) Maturation of spontaneous firing properties after hearing onset in rat auditory nerve fibers: spontaneous rates, refractoriness, and interfiber correlations. *J Neurosci* 36:10584–10597.
- Wu X, Liao L, Liu X, Luo F, Yang T, Li C (2012) Is ZD7288 a selective block of hyperpolarization-activated cyclic nucleotide-gated channel currents? *Channels* 6:438–442.
- Yamada R, Kuba H, Ishii TM, Ohmori H (2005) Hyperpolarization-activated cyclic nucleotide-gated cation channels regulate auditory coincidence detection in nucleus laminaris of the chick. *J Neurosci* 25:8867–8877.
- Yi E, Roux I, Glowatzki E (2010) Dendritic HCN channels shape excitatory postsynaptic potentials at the inner hair cell afferent synapse in the mammalian cochlea. *J Neurophysiol* 103:2532–2543.
- Yoshimoto R, Iwasaki S, Takago H, Nakajima T, Sahara Y, Kitamura K (2015) Developmental increase in hyperpolarization-activated current regulates intrinsic firing properties in rat vestibular ganglion cells. *Neuroscience* 284:632–642.